Montanuniversität Leoben

Diploma Thesis

Synthesis and Characterisation of DC-Magnetron Sputtered Molybdenum Oxide Thin Films

by

Christoph Jachs

This Thesis has been carried out at the Chair of Functional Materials and Materials Systems at the Department of Physical Metallurgy and Materials Testing, Montanuniversität Leoben, Austria, in Cooperation with PLANSEE SE, Reutte, Austria.

Leoben, March 2015

Affidavit

I declare in lieu of oath, that I wrote this thesis and performed the associated research myself, using only literature cited in this volume.

Leoben, March 2015 Christoph Jachs

Acknowledgement

I am indebted to all those without whose help this thesis would not exist.

Thus, I want to express my sincere gratitude to Univ.-Prof. Dipl.-Ing. Dr.mont. Christian Mitterer, Head of the Chair of Functional Materials and Materials Systems at the Montanuniversität Leoben, Austria for the opportunity to write this thesis at his Chair.

I want to thank Dipl.-Ing. Julia Pachlhofer for the supervision of this thesis. I also want to thank her, Dipl.-Phys. Dr.mont. Robert Franz and Prof. Mitterer for the thorough read troughs and corrections of the manuscript.

I want to thank all members of the thin film group for the collegial atmosphere, but especially Mag. Velislava Terziyska and Dipl.-Ing. Anna Hofer for their support and their help at any time, further for their patience, their instructions and briefings for all kind of equipment and software.

I want to thank Ing. Karl-Heinz Pichler for his technical advice and support.

I also want to thank Michaela Zabernig at PLANSEE SE for providing the EDS and WDS measurements as well as the SEM images.

My deepest gratitude belongs to my family.

Table of Contents

1 INTRODUCTION

Electronic displays are an indispensable product in today's modern information society. They are part of various small portable electronic devices, such as smartphones, tablets, notebooks, personal digital assistants (PDAs) etc. and they are also used as television screens and desktop computer monitors. The introduction of flat-panel display technologies (i.e. plasma panels, liquid crystal displays (LCDs)) revolutionised the availability of "pocket-devices" and ultimately displaced the old cathode ray tubes. Today, LCDs are a widely used kind of displays also because of their longer lifetime and lower power consumption compared to plasma-panels [1].

The imaging process is controlled by electronic components consisting of materials which shall combine good electrical conductivity and optical transparency. Such a behaviour is mainly limited to certain groups of metallic oxides [2]. As the dominating material so-called tin doped indium oxides (ITO) are prevalent. They are used as electrode materials in flat-panel displays which are mainly based on thin film structures [3].

Since the availability of ITO is limited due to the expensive indium, alternative material solutions for electrode materials are being explored, e.g. molybdenum oxides. They are known to exhibit a huge variety in electrical and optical properties depending on their oxidation state. At their lowest oxidation state MoO_2, they have an opaque appearance and show a metal-like conductivity while at their highest oxidation state MoO_3, they are transparent and electrically insulating. Within the system molybdenum-oxygen, the occurrence of additional line phases between MoO_2 and MoO_3 was reported [4]. Their electrical conductivity ranges from metallic to a semiconducting behaviour at room temperature [5] and they exhibit different colouring [6, 7]. This variety in tuneable properties has attracted a lot of scientific interest to this group of materials. As a result, molybdenum oxide thin films have been explored for use in gas sensing applications [8–10], as an anode material for aqueous micro-supercapacitors [11], for micro-batteries [12], display panels, solar cells [13] and electronic devices [14].

This thesis follows the approach of synthesising molybdenum oxide thin films by reactive and non-reactive DC magnetron sputter deposition. Its focus is on the investigation of the formed molybdenum oxides and on possible differences in results achieved by the two deposition techniques. Therefore, a general analysis of relevant properties of the as-deposited molybdenum oxide thin films is conducted by performing X-ray diffraction (XRD), Raman spectroscopy, energy and wavelength dispersive X-ray spectroscopy (EDS, WDS) as well as electrical resistivity, residual stress and nanoindentation measurements. Their film morphology is described by scanning electron microscopy (SEM) images.

2 THEORY

2.1 Thin Film Formation

2.1.1 Nucleation and Film Growth

The film formation can generally be divided into five steps which are nucleation, nuclei growth, coalescence, channelling and agglomeration [15, 16]. When atoms hit a substrate surface they can either be reflected or adsorbed. The adsorption depends on many parameters, but first of all it is an activation energy driven process. The incoming atoms have to transfer enough energy to the surface lattice in order to condense and to avoid desorption or re-evaporation. Once condensed, the interaction forces between adsorbed atom and the solid surface have to be strong, but the atoms should have enough mobility to diffuse along the surface. Thus, their kinetic energy is important as it can enable surface diffusion processes. Due to these diffusion processes and ongoing condensation, nuclei with critical nucleation radii are formed along the surface. The nuclei can merge to islands which then can coalesce to even larger clusters. Between connected clusters, channels can still exist that in the end vanish due to agglomeration of the film. The transport mechanisms can be regarded as an interaction of diffusion processes as well as condensation reactions [15]. The driving force of the film formation reactions is the desire to minimise the surface energy [15]. The nucleus density is an important parameter as a high nucleus density leads to a strong adhesive bonding of the film as well as a low density of defects, which then leads to a dense coating [16]. The nucleus density can be influenced by the deposition process [16].

2.1.2 Structure Zone Models

The microstructure of films obtained by physical vapour deposition (PVD) techniques is mainly influenced by the bonding strength between the adsorbed atoms and the substrate (for the first few monolayers), diffusion processes and shadowing effects due to the surface roughness which leads to a porous film structure [16]. They are directly related to activation energies and the kinetic energy of the adsorbed atoms. Thus, the mobility of the adatoms plays the major role in the film formation process and it governs the appearance of the physical structure.

Movchan and Demchishin investigated the development of the microstructure as a function of the reduced temperature T/T_m (T substrate temperature, T_m melting point of the condensed materials) for various metals and metal oxides [17]. Their findings were summarised in a structure zone model, a tool to describe the microstructure. Within this model three characteristic zones are distinguished, as shown in Figure 2.1.

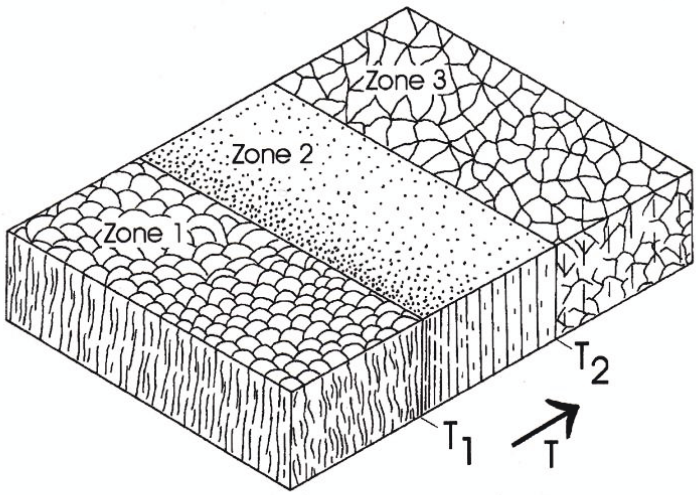

	Zone 1	Zone 2	Zone 3
Metalle T/T_m	< 0,3	0,3 ... 0,45	> 0,45
Oxide T/T_m	< 0,26	0,26 ... 0,45	> 0,45

Figure 2.1: Structure zone model after *Movchan and Demchishin* [17].

Zone 1 is characterised by a rather porous structure with a high density of defects. Shadowing effects during film growth prevail and are not equalised by diffusion due to the low temperature and, hence, missing activation energy. As a result, the grains form a domed or upside-down-like tapered structure as it can be seen in the cross section of the zone. The domes grow larger with increasing temperature. Above the first transition temperature T_1, the structure changes to a columnar one, where the columns have lower diameters than the domes. Equally to Zone 1, the structure of Zone 2 coarsens with increasing temperature as the cross section indicates. This zone exhibits a much higher density due to activation of surface diffusion processes. Finally, above the second transition temperature T_2, Zone 3 is formed having the largest crystals. It exhibits a high density and equiaxed crystals due to dominant volume diffusion. The structure of Zone 3 is a re-crystallised one.

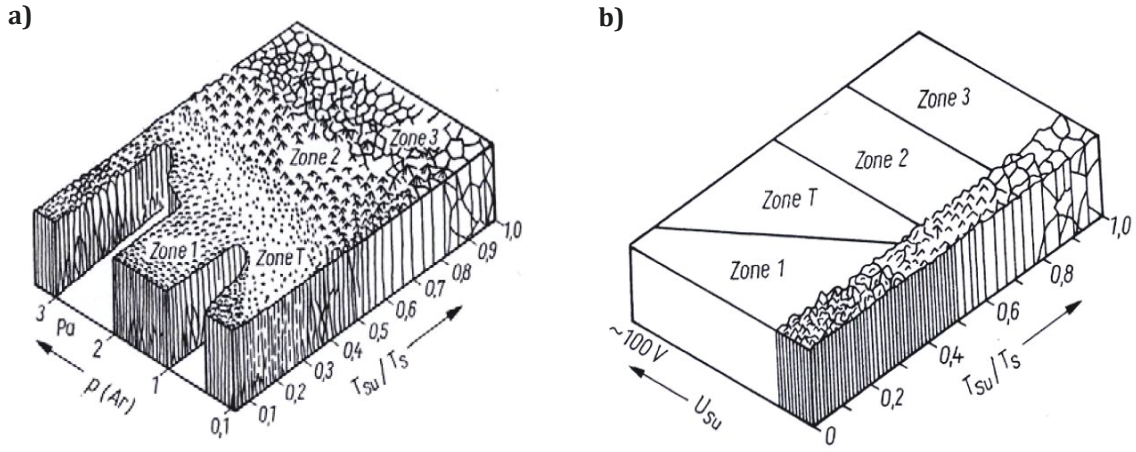

Figure 2.2: Structure zone model after a) *Thornton* [18] and b) *Messier et al.* [19].

Thornton extended the model by adding the Ar pressure as a new variable leading to a slightly modified structure zone model as shown in Figure 2.2a [18]. Between Zone 1 and Zone 2 a transition zone (Zone T) is introduced. This zone is characterised by a dense fibrous structure formed by surface diffusion. Further, both transition temperatures increase with increasing Ar pressure due to the interaction of gas atoms and adatoms.

Based on the findings of [17] and [18], *Messier et al.* investigated the influence of the bias voltage on the microstructure of thin films and extended the structure zone model, as can be seen in Figure 2.2b [19]. The bias voltage causes the attraction of ions to the substrate. Due to this bombardment more nucleation sites are generated and additional kinetic energy is transferred to the adatoms, resulting in a higher mobility and a denser structure. Thus, the bias voltage mainly influences the low temperature region (Zone 1 and Zone T) when diffusion by thermal processes is marginal.

2.2 Sputter Deposition

2.2.1 Fundamentals

Sputter deposition is one of the most important PVD techniques. The working principle and ongoing interactions that take place during deposition are schematically shown in Figure 2.3.

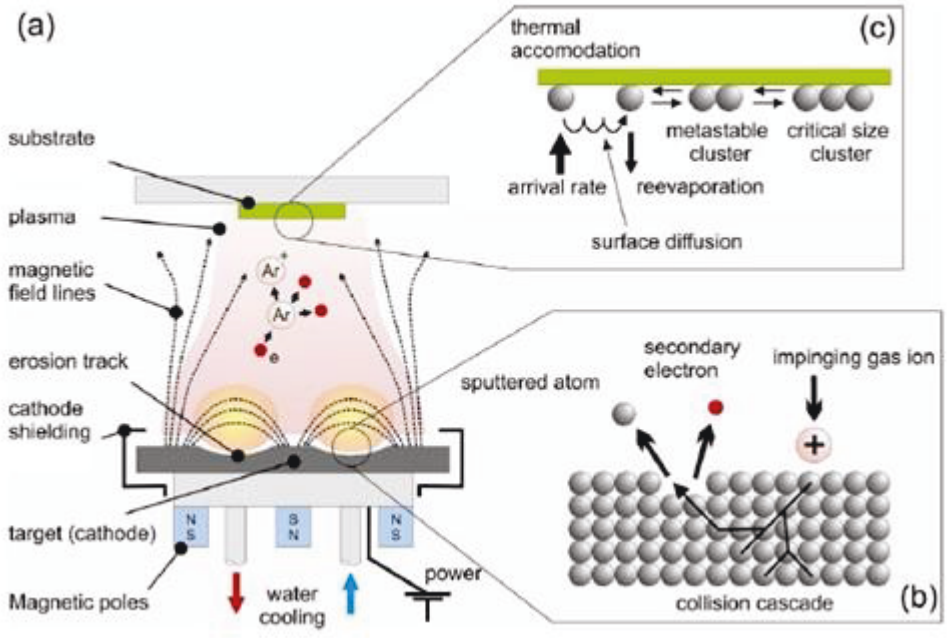

Figure 2.3: a) Schematic principle of an unbalanced magnetron sputtering system, b) interaction of bombarding ion and target and c) condensation and nucleation process at the substrate surface (adapted from [20]).

In sputter deposition, high-energetic inert gas ions, commonly Ar^+ ions, bombard a target surface causing target atoms to be ejected out of the target material due to momentum transfer. The ions used for target bombardment typically originate from a plasma, which is a quasi-neutral gas consisting of atoms, positive (and negative) ions and electrons. A working gas, such as Ar, is released into the vacuum chamber and a glow discharge is ignited due to a high voltage applied between the target (cathode) and the chamber walls (anode), as it is shown in Figure 2.3a. The ionisation of the gas is based on electron-atom collision events, where photons are released during recombination (and de-excitation) leading to the typical plasma glow. The momentum transfer of the impinging gas ions leads to a collision cascade within the target material, so that eventually atoms are ejected (see Figure 2.3b). These atoms now move through the chamber and can condensate on a substrate or the chamber walls (see Figure 2.3c). Sputtering takes place in an evacuated chamber under high vacuum conditions. This is necessary to achieve a high mean free path for the particles involved.

The sputter process can be influenced by a series of parameters. For example, in order to locally improve the target erosion by enhancing the plasma, magnets are placed behind the cathode (so-called magnetrons). Their magnetic field lines influence the electron paths (Lorentz force) and increase the amount of collision events as electrons are trapped near the target surface. In general, balanced and unbalanced magnetrons can be

distinguished. In a balanced magnetron, the magnetic field lines are closed and concentrated in the vicinity of the target. As a result, the plasma is only located near the target surface. In an unbalanced system, some field lines are open so that the plasma can extend to the substrates as well. To enhance film formation, it is also possible to apply an additional bias voltage at the substrate that attracts positive ions, which leads to the above mentioned ion bombardment and the creation of more nucleation sites for the film. More information about sputter deposition and the related plasma physics can be found in [15, 16, 21, 22].

2.2.2 Reactive Sputter Deposition

Reactive sputter deposition is used to deposit chemical compounds, such as oxides, nitrides, carbides and sulfides when sputtering metallic targets [23]. The synthesis of these compounds is enabled by adding a reactive gas, such as oxygen or nitrogen, to the inert argon working gas. The main advantage of this method is that the stoichiometry of the film can be tuned by varying the partial pressure of the reactive gas [16]. The reactions that form the chemical compounds take mostly place at surfaces, like substrates or the chamber wall and occur less frequently in the gaseous state of the reaction partners [24]. The variation of the reactive gas flow leads to several phenomena that can be understood by discussing the pressure hysteresis curve as exemplified in Figure 2.4 for an Al target sputtered in an oxygen containing atmosphere.

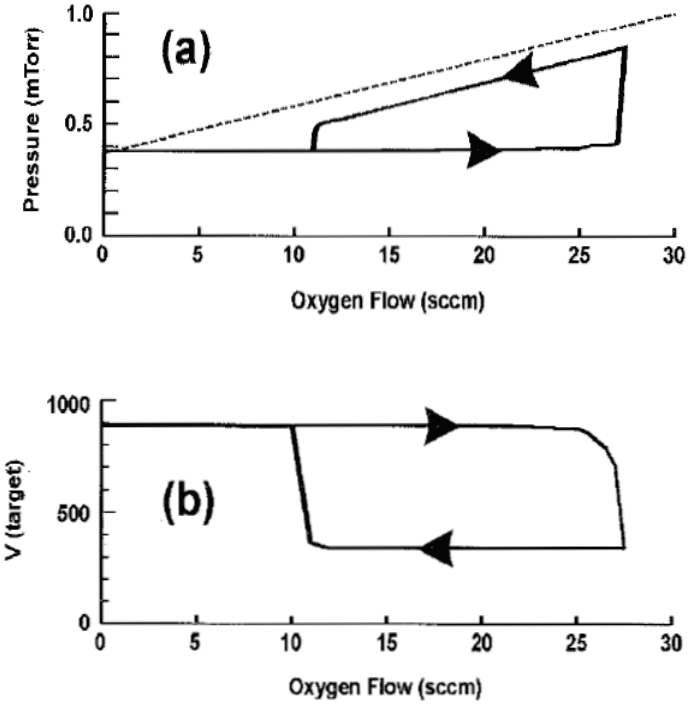

Figure 2.4: a) Pressure and b) voltage hysteresis shown for an Al target sputtered in an oxygen containing atmosphere [24].

It can be seen that the gas pressure stays almost constant over a wide range of oxygen flow. This means that enough Al atoms are sputtered that can react with the incoming oxygen. If no reaction occurs, the pressure would increase linearly as it is indicated by the dashed line. At a certain critical oxygen flow, the pressure increases significantly due to the fact that not enough Al atoms are available to bind the oxygen. Further, the oxygen reacts with the target surface forming oxides at the target top layers. These compounds exhibit a higher binding energy and a lower conductivity than the metallic Al and, as a consequence, less and less metallic aluminium is sputtered. With further increasing oxygen flow time, the whole target surface gets gradually covered by oxides. At that point the oxygen flow can be reduced and so the oxide compounds are sputtered from the surface. However, removing of the oxides from the target surface is not an instant process and the oxygen flow has to be reduced to a lower level, as compared to the flow needed for formation of the oxides. Afterwards, more and more metallic Al is sputtered again, which reacts with the oxygen and so the pressure decreases. In the end, the whole target surface is again metallic and the pressure has reached the starting point of the obtained hysteresis curve [24].

The forming of chemical compounds on the target surface by the reactive gas is called poisoning. Poisoning directly influences the sputter and deposition rate. The more a target is poisoned the lower is the deposition rate [24].

2.2.3 Compound Targets

A compound target consists of two or more elements that exhibit chemical bonds to each other. Their main advantage is that they offer the possibility to deposit films with the same composition as the target material and to use a single magnetron to deposit multi-element films [24]. When one element of the compound is preferably sputtered, the target surface becomes enriched in the other one. Such a behaviour has also been reported for metal oxide targets, where the target surface gets depleted of oxygen [16]. When the target surface is enriched in one element due to its lower sputter yield, its sputter rate increases till the sputtered flux is similar to the composition of the target material [24]. Therefore, the film typically has the same composition as the target material, but in practice differences can occur due to other factors. For instance, the difference in mass of the elements affects the transport times to the substrate. Further, different sticking coefficients and thermally activated diffusion within the target can alter the sputter flux [24]. It has been reported for a sputtered NiO target that the deposited films were deficient in oxygen [24]. This is explained by the lower sticking coefficient of the oxygen so that it is desorbed from the substrate [24]. Thus, O_2 is added to the working gas to enhance the reactivity [24].

Depending on the composition of the target, it can either be electrically conductive or insulating. For an insulating target, the radio frequency (RF) sputtering technique can be used where an AC signal is applied between the two electrodes. Above 50 kHz, the light electrons are still able to follow the high-frequency field and exhibit enough energy to ionise the working gas. The higher mobility of the electrons leads to a negative charge at the target and so ions are attracted for bombardment. The target area shall be smaller than the one of the counter electrode for efficient sputtering of the target [23, 24].

2.3 Molybdenum Oxides

2.3.1 Overview

Comparing the molybdenum-oxygen phase diagrams shown in Figure 2.5, it can be seen that both experimental [25] and theoretical [26] approaches are in good agreement within the shown temperature regions. In Figure 2.5b, the phase regions above 1700°C are also illustrated. At 2200°C, there is a eutectic point between Mo and MoO_2. According to the phase diagram shown here, no oxide phase between Mo and MoO_2 exists. However, *Schönberg* [27] reported the observation of Mo_3O, but this oxide could not be prepared in a pure state. Further attempts by different researchers to reproduce Mo_3O were unsuccessful [25]. Between the lowest oxidation state MoO_2, and the highest oxidation state MoO_3, several intermediate line phases occur which are also referred to as Magnéli phases. The intermediate phase Mo_4O_{11} melts incongruently at ~820°C and Mo_9O_{26} at ~780°C [28]. MoO_3 and Mo_9O_{26} form a eutectic at ~775°C [28]. It should be pointed out that the Magnéli phases appear at certain oxygen contents only, but for MoO_2 and MoO_3 narrow homogeneity regions of $Mo_{1.97–2.08}$ and $MoO_{2.95–3.0}$, respectively, are reported [29].

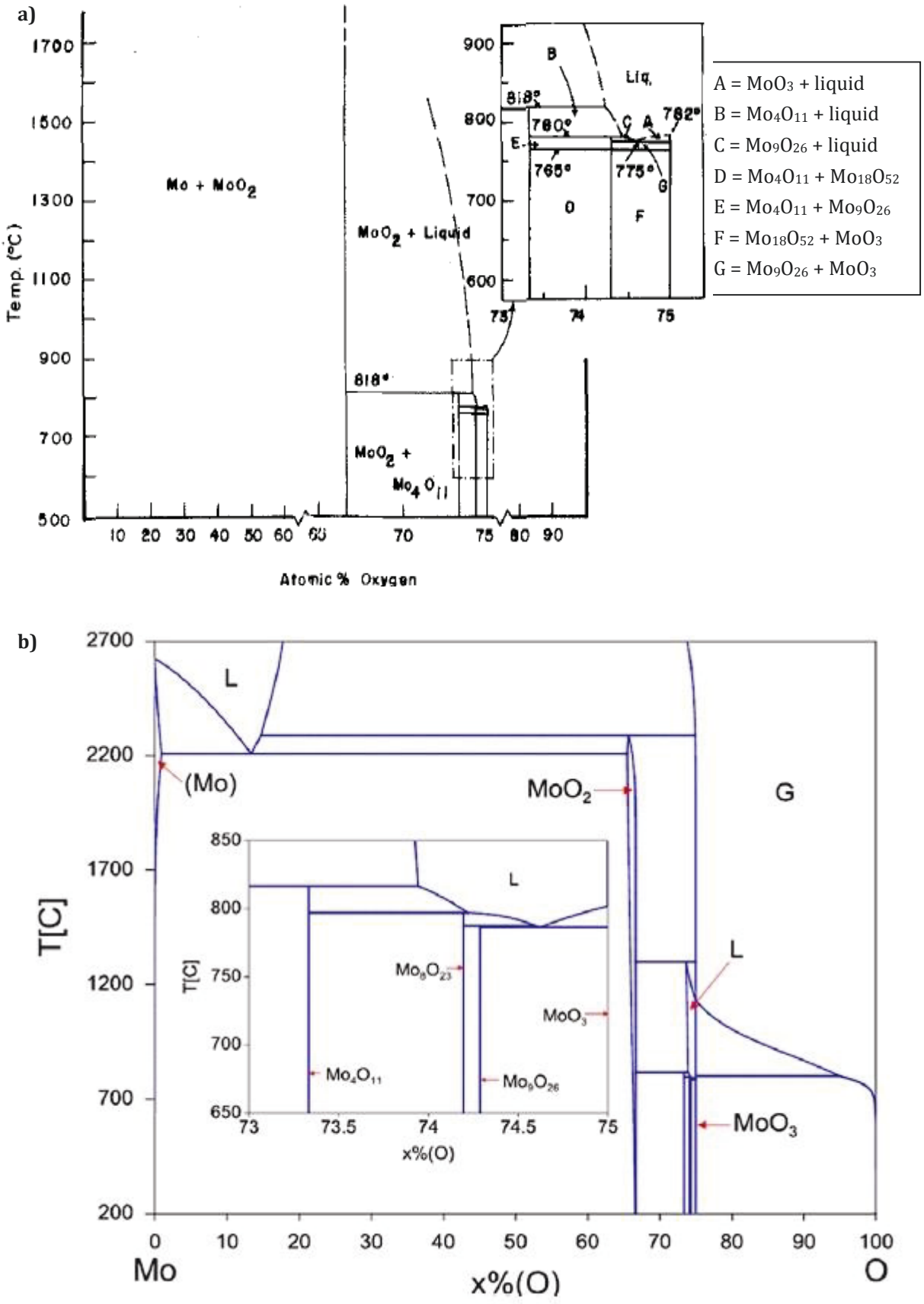

Figure 2.5: a) Experimentally obtained molybdenum-oxygen phase diagram [25] and b) the calculated binary system [26].

Solid molybdenum shows a very low solubility for oxygen in the thermodynamic equilibrium. Even at 1900°C less than ~139 ppm of oxygen are dissolved [28]. Thus, oxygen tends to segregate to the molybdenum grain boundaries causing intergranular embrittlement [30].

The Magnéli phases are defined as oxygen-deficient oxides. They are commonly part of a homologous series, e.g. Me_nO_{3n-1} [31]. The existence of such phases is not restricted to Mo, but seems to be widespread within the transition metal group, e.g. W, Ti and V. Representatives of the molybdenum oxide Magnéli phases are: Mo_4O_{11}, $Mo_{17}O_{47}$, Mo_5O_{14}, Mo_8O_{23} and Mo_9O_{26} (ranked by increasing oxygen content). Mo_4O_{11} and Mo_9O_{26} appear in two modifications [4]. The triclinic Mo_9O_{26} is also called $Mo_{18}O_{52}$. The properties of the molybdenum oxides are summarised in Table 2.1 and their stability regions are graphically shown in Figure 2.6.

Table 2.1: Selected properties of the molybdenum oxides [4-6, 32-34].

	MoO_2	Mo_4O_{11}	Mo_4O_{11}	$Mo_{17}O_{47}$	Mo_5O_{14}	Mo_8O_{23}	$Mo_{18}O_{52}$	Mo_9O_{26}	MoO_3	MoO_3
		$MoO_{2.75}$	$MoO_{2.75}$	$MoO_{2.76}$	$MoO_{2.8}$	$MoO_{2.88}$	$MoO_{2.89}$	$MoO_{2.89}$		
		η-Oxide	γ-Oxide	κ-Oxide	θ-Oxide	β-Oxide	ζ-Oxide	β'-Oxide	α-MoO_3	β-MoO_3
Crystal Structure	monoclinic	monoclinic	ortho-rhombic	ortho-rhombic	tetragonal	monoclinic	triclinic	monoclinic	ortho-rhombic	monoclinic
$T_{formation}$ [°C]		< 615	> 615	< 560	470 - 530	650 - 780	600 - 750	750 - 780		
Density [g/cm^3]	6,47	4,17	4,18	4,72		4,32	4,74	4,26	4,7	4,7
Resitivity [Ωcm]	8×10^{-5} (metallic)	0,2	0,25	< 0.05		1,2	250	3,7	~10^7 (insulating)	~10^{10} (insulating)
$T_{decomposition}$ [°C]	1100	-	815 (MoO_2 + MoO_3)	630 (γ + β)	530 (κ + MoO_3)	785 (γ + MoO_3)	550 (η + MoO_3)	785 - 800 (γ + MoO_3)	795	795
$T_{transformation}$ [°C]	-	655 (γ)	550 (η)	-	-	-	760 - 780 (β')	-	-	-

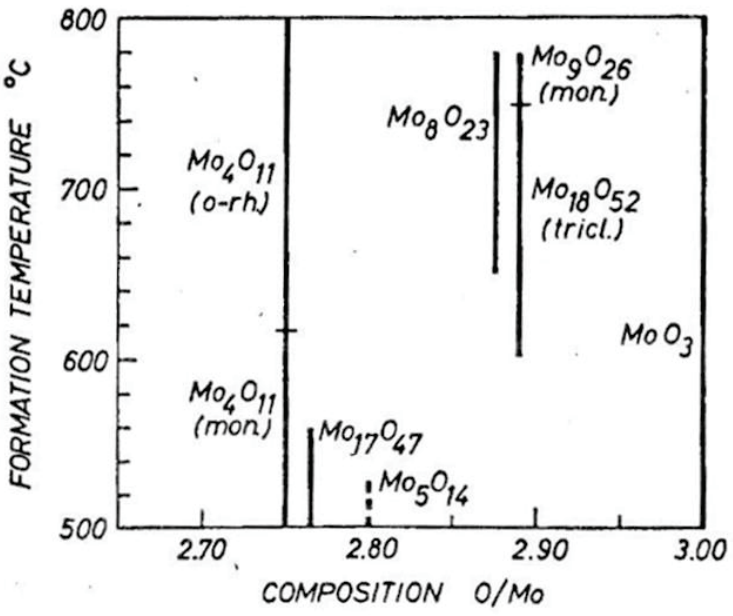

Figure 2.6: Formation diagram of the molybdenum oxides (except of MoO_2) [6].

In literature, the values for the electrical resistivity vary, which may be due to different growth and measurement methods. From Table 2.1 it can be seen, that only the two dimorphic Magnéli phases Mo_4O_{11} and Mo_9O_{26} undergo transformation processes. The transformation from γ-Mo_4O_{11} to η-Mo_4O_{11} and vice versa is a slow process that takes several weeks at temperatures between 550°C and 655°C [4]. The change from triclinic to monoclinic Mo_9O_{26}, on the other hand, takes place within two hours at 780°C [4]. Further, it can be seen that the β and β' phases decompose into the same oxides. Finally, also Mo_5O_{14} seems to be a metastable phase [35].

2.3.2 MoO_2

MoO_2 represents the lowest oxidation state of the molybdenum oxides exhibiting an oxygen content of 66.7 at.%. Its crystal structure can be described as based on a deformed rutile type, as it is indicated in Figure 2.7 [36].

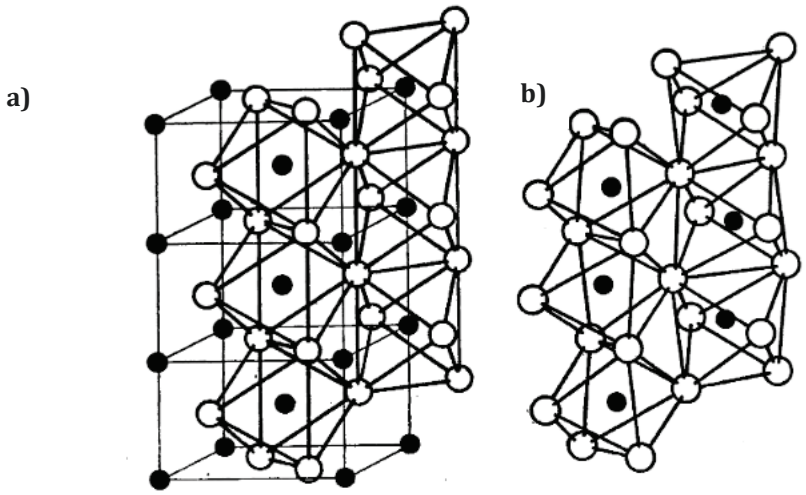

Figure 2.7: a) The ideal rutile structure versus b) the MoO_2 structure [36].

The building elements are MoO_6 octahedra sharing edges and corners. The distortion is caused by the Mo atoms, which alternatingly form metal-metal doublets with direct metal-metal bonds. This is also the reason for the metal-like conductivity of MoO_2 of about 10^{-4} to 10^{-5} Ωcm [5, 34] (compared to Mo of 5.6×10^{-6} Ωcm at 293 K [37]). Due to the doublets, the d_{11} electron band is split and the metal-metal σ bonding is filled up by one d-electron, while the second one partially fills the metal-oxygen π^* band [38, 39]. Concerning its optical appearance, it is opaque with a reddish brown, reddish purple colouring [6, 7].

2.3.3 MoO_3

The molybdenum oxide with the highest oxidation state, MoO_3, appears in two modifications: Either as α (orthorhombic) or β (monoclinic) structure where the former is the thermodynamically stable one [40].

α-MoO_3 (because of its orthorhombic structure also referred to as o-MoO_3) is composed of distorted MoO_6 octahedra forming a layered structure of two levels each. The levels are connected by the mutually shared octahedral edges. This leads to zig-zag rows in the [001] direction, as shown in Figure 2.8 [6, 41].

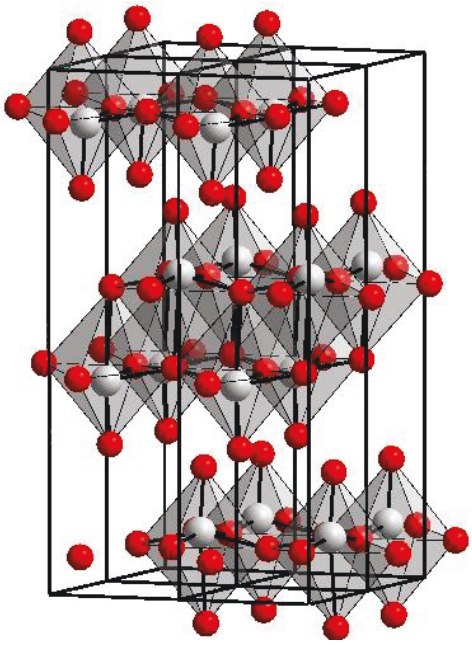

Figure 2.8: Layer structure of α-MoO_3 [42].

MoO_3 is a diamagnetic insulator. All metal-oxygen bonding orbitals are filled and, therefore, no more electrons are left to fill up the empty energy states in the metal d-conduction band [43]. The band gap is around 3 eV for both modifications [34]. As a result, both modifications are transparent and appear slightly yellowish [34, 44].

2.4 Thin Film Transistor – Liquid Crystal Displays

Among the various LCD technologies, the thin film transistor (TFT) -LCD is the dominant one [45]. Since the electrodes are arranged like a matrix, this structure is also referred to as active matrix LCD (AMLCD). As it is shown in Figure 2.9a, the display basically consists of two glass plates that sandwich the liquid crystals. On the glass, various electronic components are placed, for example the pixel and counter electrodes that are responsible

for the orientation of the liquid crystals [1]. Additionally, transistors and conductive paths are in contact with the electrodes in order to control pixel generation. It is important that the structures on the glass substrate have similar optical transmittance as the glass and low reflectivity to avoid irritation of the image.

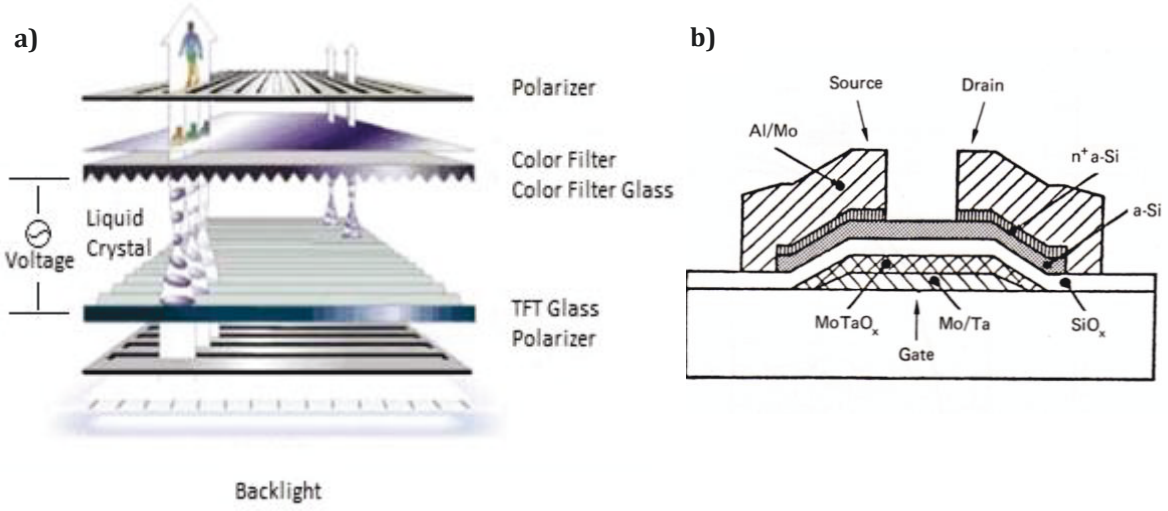

Figure 2.9: a) Schematic setup of a TFT-LCD [46] and b) schematic cross-section of an amorphous Si TFT [3].

The thin film transistors are composed as a multilayer structure as illustrated in Figure 2.9b. They are contacted via transparent conductive oxide (TCO) pixel electrodes and act as ON/OFF switches, thus driving the active matrix [3]. The contact is realised by metallic bridges normally made of molybdenum alloys (e.g. Mo-Ta), where the Ta increases the corrosion resistance in humid environment [47, 48]. New approaches use layer structures based on MoO_x or $MoTaO_x$ and additional metallic films for improved visual performance [48].

Tin doped indium oxide (ITO) represents the best known group of TCO materials and they are presently dominating the use as electrodes in LCDs [3]. ITO is a semiconductor material with a band gap of around 3.75 eV leading to good transparency in the visual light spectrum [3]. The good electrical conductivity is caused by tin doping, where In^{3+} is substituted by Sn^{4+} resulting in the formation of a degenerated n-type semiconductor [3]. More detailed information about the various LCD technologies in general can be found in [45, 49], about TFT technology in particular in [50] and about ITO in [2, 3].

3 Experimental Details

3.1 Coating Synthesis

3.1.1 Substrates and Targets

All thin films investigated in this thesis were grown on silicon (n-type (phosphorus), (100) orientation, 20 mm × 6 mm, 325 µm thickness, single side polished) and glass (window glass, 20 mm × 6 mm × 1 mm) substrates. The substrates were cleaned in an ultrasonic bath for five minutes, each in acetone and ethanol prior to the deposition process.

In total, three different target compositions were used in two different sputtering systems. In the first system, two molybdenum targets (99.95% purity, ∅ 50.4 mm) were sputtered in reactive atmosphere (Ar and O_2). In the second sputtering system, one MoO_2 target consisting of MoO_2 with Mo_4O_{11} impurities and one MoO_x target (50 mol% MoO_2 and 50 mol% MoO_3), both with diameter of 75 mm, were used in non-reactive atmosphere (Ar). All targets were produced powder metallurgically by PLANSEE SE.

3.1.2 Sputter Deposition Systems

Figure 3.1 shows the laboratory scale sputter deposition system used for the deposition of those films reactively sputtered in Ar and O_2 atmosphere. It consists of a vacuum chamber with an internal dimension of ∅ 305 mm × 410 mm and three unbalanced magnetrons. On top of these magnetrons, the targets are located which can be covered individually by shutters (see Figure 3.1c). Opposite to the targets, the sample holder is placed which can be heated from its backside by two halogen lamps of 1 kW each. The discharge voltage is applied by three ENI MKS RPG-50 generators that can be used in DC as well as asymmetric bipolar pulsed DC mode. Two generators regulate the target power supply, while the third one applies a bias voltage to the substrates. Additionally, the sample holder can be rotated for a homogenous temperature distribution and deposition rate. The chamber was evacuated by a dual stage rotary vane pump (Pfeiffer Duo 20) and a turbomolecular pump (Pfeiffer TMH 521 P).

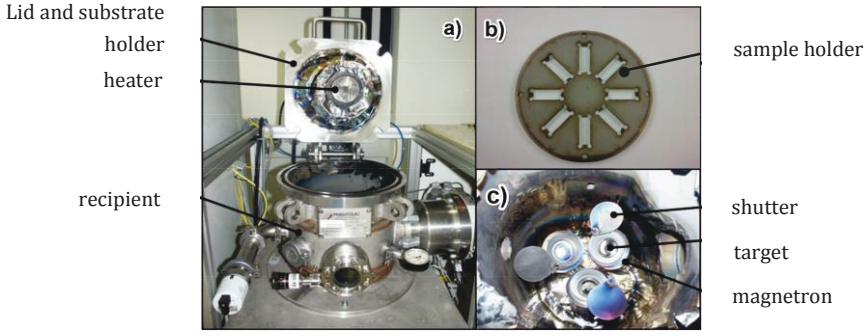

Figure 3.1: Deposition system for the reactively sputtered thin films (adapted from [51]).

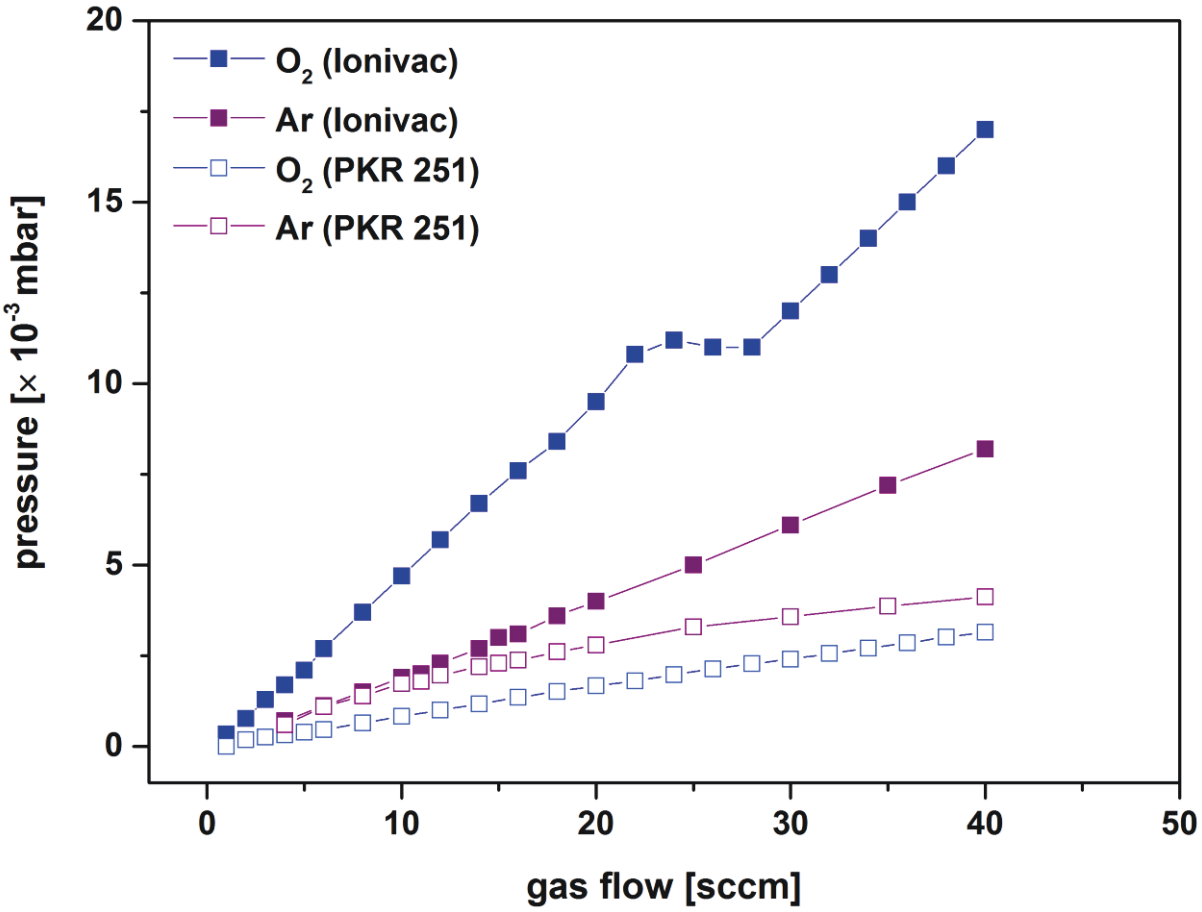

Figure 3.2: Calibration curves of Ar and O_2 for the device where the reactive sputter depositions were conducted. The calibration was performed in November 2011 (modified after [52]). The designations Ionivac and PKR 251 refer to the pressure gauges used.

The pressure calibration curves of the two gases argon and oxygen for the previously described deposition device are shown in Figure 3.2. Due to the fact that Ar/O_2 gas mixtures were used in that sputter device to synthesise the films, the oxygen partial pressure is a crucial factor that influences the film properties. The total gas pressure in the chamber was measured with a compact full-range gauge (Pfeiffer PKR 251). Since that measuring cell has an accuracy of ~±30% and a reproducibility of ~±5% within the measurement region used [53], the calibration curves obtained by a hot cathode gauge (Oerlikon Ionivac) were taken for calculation because of its double accuracy of ±15% and its reproducibility of ±5% [54].

The distance between target and sample holder was 55 mm, while the target was tilted by 13.3° in relation to the sample holder. The rotation speed of the sample holder was set to 80 rpm. After evacuation, the chamber was baked out at 500°C for 30 min and subsequently cooled down to the deposition temperature of 120°C. Then the Mo targets were sputtered in argon atmosphere for approximately 1-2 min by applying a 0.35 A DC current (~110 W) to each of the two magnetrons to clean the target surfaces. After target cleaning, the shutters were opened and all depositions were conducted in reactive atmosphere for 30 min with unaltered current and a total gas pressure of approximately 4×10^{-3} mbar. Additionally, a pulsed substrate bias voltage of –50 V (pulse frequency 250 kHz with a positive pulse of +37 V and a positive pulse duration of 0.5 µs) was provided for all reactive sputter depositions. In order to investigate the influence of the oxygen content on the deposited films, the oxygen flow was altered while keeping the total gas flow of ~40 sccm constant. In addition, experiments with shorter deposition times were conducted to study the change of the film properties in dependence on the film thickness. Detailed process parameters are listed in Table 3.1 with the coatings in order of increasing oxygen partial pressure p_{O2}/p_{ges}.

Table 3.1: Process parameters for the deposition runs performed in both sputtering systems.

Sample	Targets	Deposition time [min]	Ar Flow [sccm]	O_2 Flow [sccm]	p_{O2}/p_{ges} [%]
Mo - 9	2 × Mo	30	37	2.5	14.1
Mo - 7	2 × Mo	30	35	5	27.6
Mo - 8	2 × Mo	30	32	7.5	39.2
Mo - 6	2 × Mo	30	30	10	48.2
Mo - 16	2 × Mo	30	20	20	74.3
Mo - 18	2 × Mo	5.77	20	20	74.3
Mo - 17	2 × Mo	30	10	30	90.1
Mo - 19	2 × Mo	13.64	10	30	90.1
Mo - 15	2 × Mo	30	0	40	100
Mo - 20	2 × Mo	17.64	0	40	100
MoO_2 - 1	1 × MoO_2	30	10	-	-
MoO_2 - 2	1 × MoO_2	2	10	-	-
MoO_x - 1	1 × MoO_x	30	10	-	-
MoO_x - 2	1 × MoO_x	1.17	10	-	-

The experiments in non-reactive atmosphere were carried out in a modified, unbalanced Leybold Heraeus Z400 DC sputter system, as it is shown in Figure 3.3. The chamber's dimensions are ∅ 420 mm × 200 mm. A dual stage rotary vane pump (Pfeiffer Duo 20) and a turbomolecular pump (Leybold Turbovac 361) were utilised to evacuate the

chamber. In this system, only one target at a time was sputtered (either MoO_2 or MoO_x). The magnetron as well as the target were placed parallel in relation to the sample holder and their distance was approximately 50 mm.

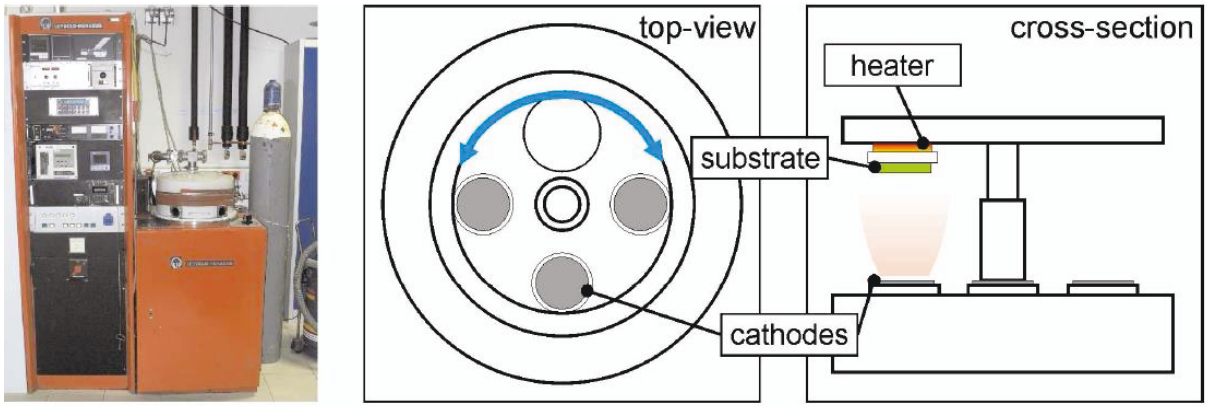

Figure 3.3: Schematic illustration of the sputter system as used for the non-reactively sputtered thin films [20].

Compared to reactive sputtering, the non-reactive sputter depositions were controlled by regulating the power applied to the magnetron instead of the current. Thus, the target was sputtered for several minutes at 200 W applied to the magnetron to clean the target surface prior to deposition. Afterwards the films were deposited for 30 min while the provided 200 W (~0.26 A current) remained unaltered. For deposition, the sample holder was rotated manually over the target. In all experiments, a working gas pressure of about 1.5×10^{-3} mbar was used. No additional heating (room temperature) and no substrate bias voltage was applied. The influence of the deposition time on the film properties was studied as well. These process parameters are also listed in Table 3.1.

3.2 Coating Characterisation

3.2.1 Coating Thickness

The coating thickness is required for evaluation of experimental data obtained from nanoindentation, electrical resistivity and residual stress measurements. It further gives information on the growth kinetics and deposition rate and it affects optical properties, density of defects and stress levels.

In this thesis, the ball cratering method (see Figure 3.4) using a CSM CaloWear test was applied to determine the thickness of the films deposited on silicon substrates. To calculate the film thickness, the following reduced equation is applicable [56]:

$$t_c = \frac{D_o{}^2 - D_i^2}{4D}, \tag{1}$$

with the outer and inner diameter of the calotte D_o and D_i, respectively, the ball's diameter D and the coating thickness t_c. The calotte is generated by grinding with a rotating steel ball covered with diamond suspension that is in contact with the specimen's surface. Subsequently, the dimensions of the calotte are measured with a light optical microscope.

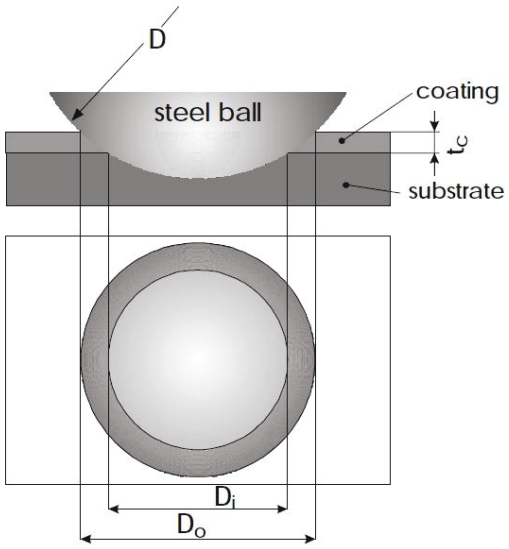

Figure 3.4: Scheme of the ball cratering method and generated calotte [55].

3.2.2 Chemical Composition

EDS and WDS measurements were performed on films that were deposited on silicon substrates in order to analyse their chemical composition. They were conducted with an Octane Plus silicon Drift Detector at PLANSEE SE.

The simultaneous measurement of the concentration of a light and heavy element via characteristic X-ray detection, as it is performed in EDS and WDS, is always a challenge. Here, the measurement voltage was adjusted to each film thickness in EDS to achieve the best possible result. Due to the large difference in atomic number Z for Mo and O (42 and 8, respectively), various phenomena occur that affect the measurement. For example, absorption and fluorescence events have to be taken into account [57]. Further, it has to be considered that due to the presence of Mo, the critical excitation energy is high and the excitation volume is low. The heavy Mo matrix absorbs the radiation of the light O and as

a result, a lower oxygen concentration is detected. The absorption can also lead to fluorescence, but normally this influence is neglected [58]. Additionally, due to the increasing amount of oxygen, the conductivity generally decreases and, hence, the determination of the element concentrations is difficult.

Secondary electron SEM images were taken from the films in order to describe their morphology. The images were taken at PLANSEE SE with a Zeiss NTS Ultra plus from films grown on silicon.

The state of the chemical bonds was investigated by Raman spectroscopy experiments that were performed by using a Horiba Dilor Raman spectrometer. A monochromatic laser (Nd:YAG, λ = 532.068 nm) was used in combination with a series of filters to tune the laser power in order to avoid any damage of the films. The laser power was set to 1.28 mW for the thicker films, while the thinner films (100–200 nm) were measured with 49.2 μW.

3.2.3 Microstructure

In order to analyse the occurring phases, X-ray diffraction measurements were performed for all coatings. They were carried out with a Bruker-AXS D8 Advance diffractometer applying the grazing incidence method. The angle of incidence was fixed at 2° while the detector was moving in 0.02° steps every 1.2 s. Cu-K_α radiation (λ = 0.154 nm) was used and the detector measurement range was set from 10 to 90°. The phases were identified by comparing the peak positions in the measured patterns to reference patterns in the International Centre for Diffraction Data (ICDD) database. The diffractometer was operating at 40 mA tube current and 40 kV voltage.

Based on XRD measurements, a qualitative and quantitative phase analysis is possible. Further, the lattice constant a of a cubic crystal structure, such as Mo, can be determined if the incident wavelength λ, the diffraction angle 2θ and the planes (hkl) at which diffraction occurs are known [59]. This is realised by combining Bragg's law (eq. 2) with the plane-spacing equation (eq. 3):

$$n\lambda = 2d \sin\theta\,, \tag{2}$$

$$\frac{1}{d^2} = \frac{(h^2+k^2+l^2)}{a^2}\,, \tag{3}$$

which results in:

$$\frac{\sin^2\theta}{(h^2+k^2+l^2)} = \frac{\lambda^2}{4a^2}\,. \tag{4}$$

Equation 4 combines θ and a for any given diffraction plane *(hkl)* in the cubic system [59]. It will be used later on to calculate the lattice constant of the Mo phase.

3.2.4 Electrical Resistivity

The resistivity of all coatings was measured by a Jandel four point probe. Four specimens of each deposition run were evaluated (two on-glass and two on-silicon films). For the reactively sputtered deposition run "Mo-6", only one coating on glass was available for evaluation. Each film was measured three times in the centre of the specimen. Additionally, each film was also measured near the edges of the substrate to investigate its homogeneity. Only voltage values constant over a relevant period of time were taken for further calculations. Steadily growing values were regarded as dielectric behaviour.

In the four point technique, four measurement tips are simultaneously brought in contact with the film. The working principle is schematically shown in Figure 3.5. A DC current is applied by the outer two tips, while the inner two are used to measure the voltage. The electrical resistivity ρ is calculated by the following equation [60]:

$$\rho = \frac{\pi t}{ln\,2}\left(\frac{V}{I}\right), \tag{5}$$

with the film thickness t, the voltage V and the current I.

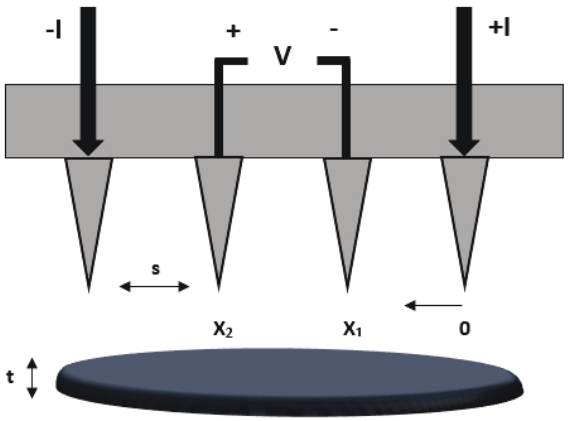

Figure 3.5: Schematic drawing of the Jandel four point probe for resistivity measurements (adapted from [60]).

3.2.5 Mechanical Properties

The hardness and Young's modulus of the coatings were determined using a UMIS nanoindenter system (Fischer-Cripps Laboratories, Berkovich indenter (tip radius approximately 150 nm)). The properties were measured for films that were grown on silicon and exhibited a thickness ≥1 µm. All experiments were evaluated using the software package IBIS. For each sample, 20 loading-unloading cycles were recorded and at least 10 were taken for evaluation.

A series of factors have to be taken into consideration when performing nanoindentation measurements on thin films. In order to avoid the substrate influence on the mechanical properties of the thin film, the "rule of thumb" that the maximum indentation depth should be ≤10% of the coating thickness is typically applied [61]. For this reason, the maximum indentation depth was adjusted for each coating. The measurements are also sensitive to surface roughness and temperature changes (thermal drift) and, thus, polishing of the film surface and a constant ambient temperature are important. The hardness and Young's modulus were determined from the load-displacement curves (see Figure 3.6) by applying the Oliver and Pharr method [62].

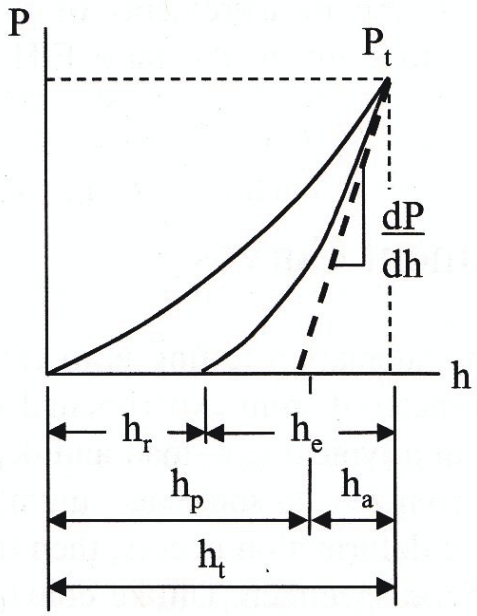

Figure 3.6: Schematic load-displacement curve obtained in nanoindentation showing the loading and unloading cycle [61].

The hardness H was calculated according to the following equation [61]:

$$H = \frac{P}{A}\left[\frac{A_i}{A}\right], \tag{6}$$

with the load P, the contact area A and the area correction function $\frac{A_i}{A}$. This function is needed for the non-ideal indenter tip shape since it wears off during indentation experiments. The Young's modulus E^* was calculated after equation 7 [61]:

$$E^* = \frac{dP}{dH}\frac{\sqrt{\pi}}{2\beta\sqrt{A}}\sqrt{\frac{A_i}{A}}, \tag{7}$$

with the indenter geometry correction factor β and the slope of the unloading curve $\frac{dP}{dH}$ at P_{max}.

Further, residual stresses were measured of all films deposited on silicon by using the wafer curvature method. All measurements were performed at room temperature. In this method, the specimen's curvature is measured to determine its residual stresses, as illustrated in Figure 3.7. Two incidental parallel laser beams (λ = 632.8 nm, beam diameter: 1.2 mm) are deflected by the specimen and redirected by a mirror. Depending on the specimen's curvature, the resulting distance of the initially parallel (d_0 = 15 mm) beams is measured. The stress σ_f is calculated after the modified Stoney equation (modified after [64]):

$$\sigma_f = M\frac{t_s^2}{6t_c}\frac{1}{R}, \tag{8}$$

with the substrate's biaxial modulus M, the substrate thickness t_s, the coating thickness t_c and the specimen's curvature R. The curvature can be determined after [63]. Thus, the following equation is applicable when the specimen is placed at the measuring plate:

$$R = \frac{2hd_o}{d_1 - d_0}, \tag{9}$$

with the distance h between film and mirror, the initial distance d_o between the two laser beams and the measured beam distance d_1 after redirection from the mirror.

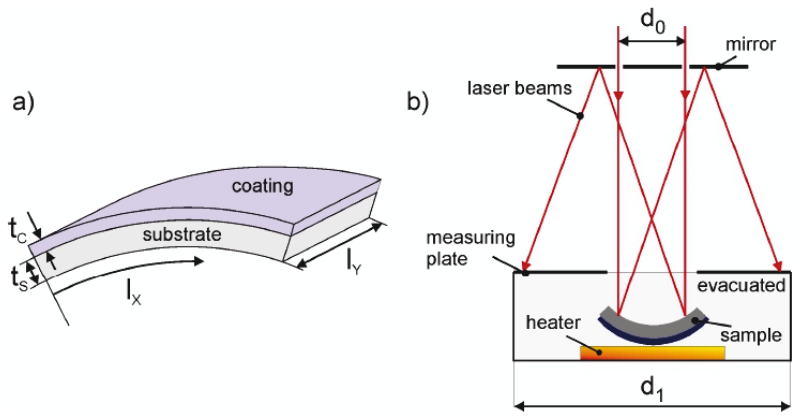

Figure 3.7: a) Specimen bending due to residual compressive stress and b) principle of the wafer curvature method (adapted from [63]).

Residual stresses are caused by various reasons. The difference between substrate and film, e.g. coefficient of thermal expansion or crystal lattice can lead to stresses, but they can also arise from the film formation process or by contaminations from the working gas. Even epitaxial films as such are not stress free due to formation defects like vacancies or dislocations [15].

4 RESULTS

4.1 Chemical Composition and Coating Thickness

The results of the EDS and WDS measurements and the coating thicknesses are listed in Table 4.1 in order of increasing oxygen flow. As expected, the oxygen content in the films generally increases with increasing oxygen flow and partial pressure. However, there are differences between the EDS and WDS results and for some coatings a lower oxygen content was measured, even though they were synthesised at higher oxygen partial pressure. This may be explained by the fact that the applied measurement voltage in EDS was adjusted to the coating thicknesses, which was not done in WDS. Further, the already discussed difficulties that arise when simultaneously measuring the concentration of a light and heavy element seem to have a significant influence on the measurements as well.

Table 4.1: The oxygen flow is shown in relation to the oxygen partial pressure (p_{O2}/p_{ges}) as well as the molybdenum and oxygen concentrations obtained by EDS and WDS measurements. In addition, the measured coating thicknesses obtained by ball cratering are added. The deposition time was 30 min for each film. The **black** values are those of the **reactively sputtered** films, the red and blue ones are for the films sputtered non-reactively from the MoO_2 and MoO_x targets, respectively.

O_2 Flow [sccm]	p_{O2}/p_{ges} [%]	Composition (EDS)		Composition (WDS)		Thickness [µm]
		Mo [at.%]	O [at.%]	Mo [at.%]	O [at.%]	
2.5	14.1	65	35	67	33	1.9
5	27.6	56	44	57	43	2.3
7.5	39.2	47	53	48	52	2.7
10	48.2	44	56	28	72	2.7
20	74.3	32	68	30	70	2.2
30	90.1	33	67	11	89	0.8
40	100	33	67	15	85	0.2
-	0	45	55	43	57	2.1
-	0	44	56	41	59	2.6

Figure 4.1 shows the evolution of the deposition rate versus the oxygen partial pressure in detail. The coating thickness increases gradually till a plateau of 2.7 µm (deposition rate 90 nm/min) is reached and then it decreases to 0.2 µm (6.7 nm/min). The reason for the increase in coating thickness lies in the addition of oxygen to the working gas, which means more atoms are available for the film formation process when the erosion rate of the target is kept constant. The decrease can be explained by poisoning of the target causing a strong decrease in deposition rate and, as a consequence, also in coating thickness since the deposition time was kept constant. In addition, the input of lighter

oxygen atoms most likely results in a decrease of the sputter yield, because the heavy inert argon ions are less and less used as the bombarding species to provide erosion of material from the target. For all these reasons, the coating sputtered in pure oxygen atmosphere exhibits the lowest coating thickness.

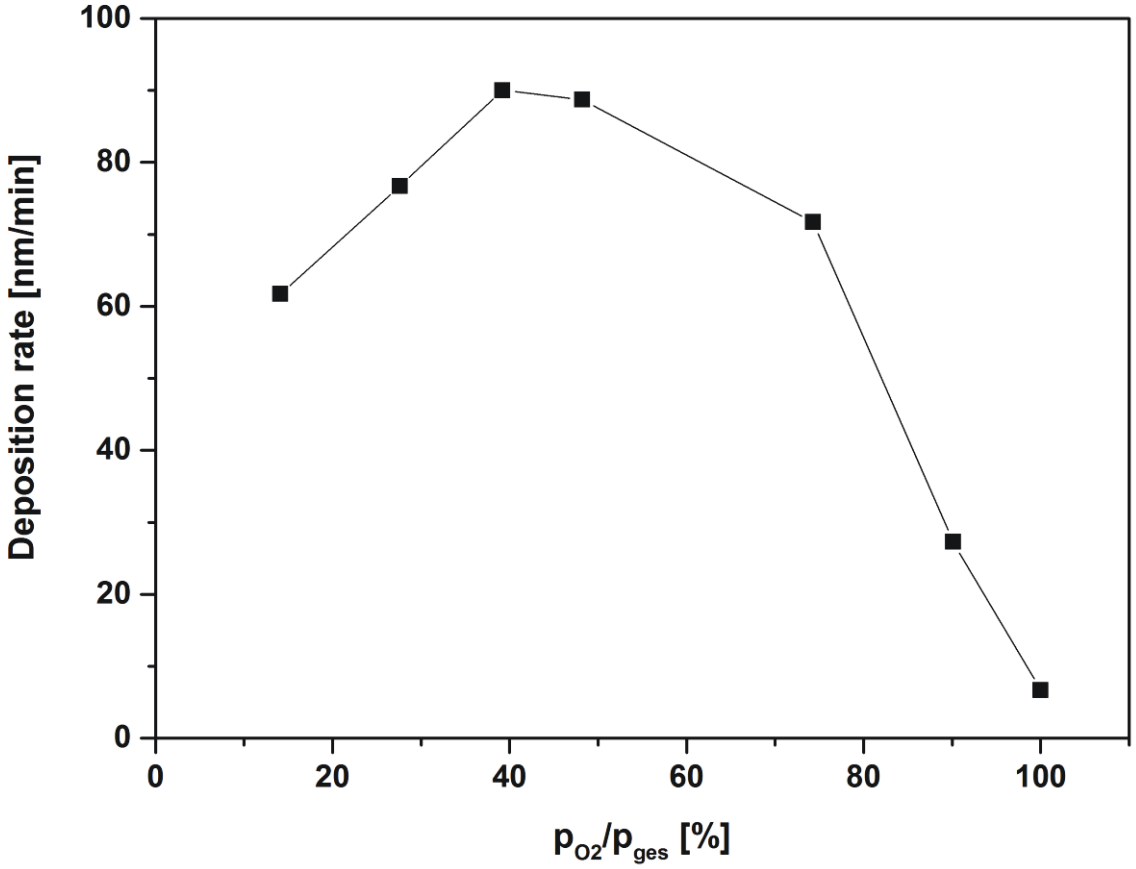

Figure 4.1: Deposition rate versus the oxygen partial pressure for the reactively sputtered films.

The non-reactively sputtered MoO_2 and MoO_x films reveal almost identical element concentrations (both EDS and WDS) and also similar coating thicknesses. In terms of chemical composition, the films are comparable to the reactively sputtered films using p_{O2} = 39.2% (EDS and WDS) and p_{O2} = 48.2% (EDS).

4.2 Raman Spectroscopy

The films deposited on silicon show almost identical Raman spectra as their equivalents deposited on glass, as it is shown in Figures 4.2 and 4.3. The dominant peak at about 900 cm^{-1} has been cut off for a better visualisation of the spectra in both figures. The broad signals detected from the films sputtered reactively with p_{O2} ranging from 14.1% to 48.2% do not allow for an unambiguous identification of the specific phases present. However, the Raman signals detected from the films with p_{O2} = 74.3%, 90.1% and 100% are generally in good agreement with the reference curve of o-MoO_3. The few peaks deviating from the reference data of MoO_3 indicate the presence of phases with other oxidation states, apart from Mo^{6+}. The specimens synthesised with p_{O2} = 74.3%, 90.1% and 100% on silicon reveal slightly different spectra than their equivalents on glass. Especially the specimen with p_{O2} = 74.3% shows five additional peaks in the Raman spectrum at 160, 338, 665, 820 and 996 cm^{-1}, which are absent in the spectrum of the film deposited on glass. Thus, there seems to be an influence of the substrate on the short-range order of the crystals due to the different crystallinity and electrical conductivity of silicon and glass. However, this influence is marginal.

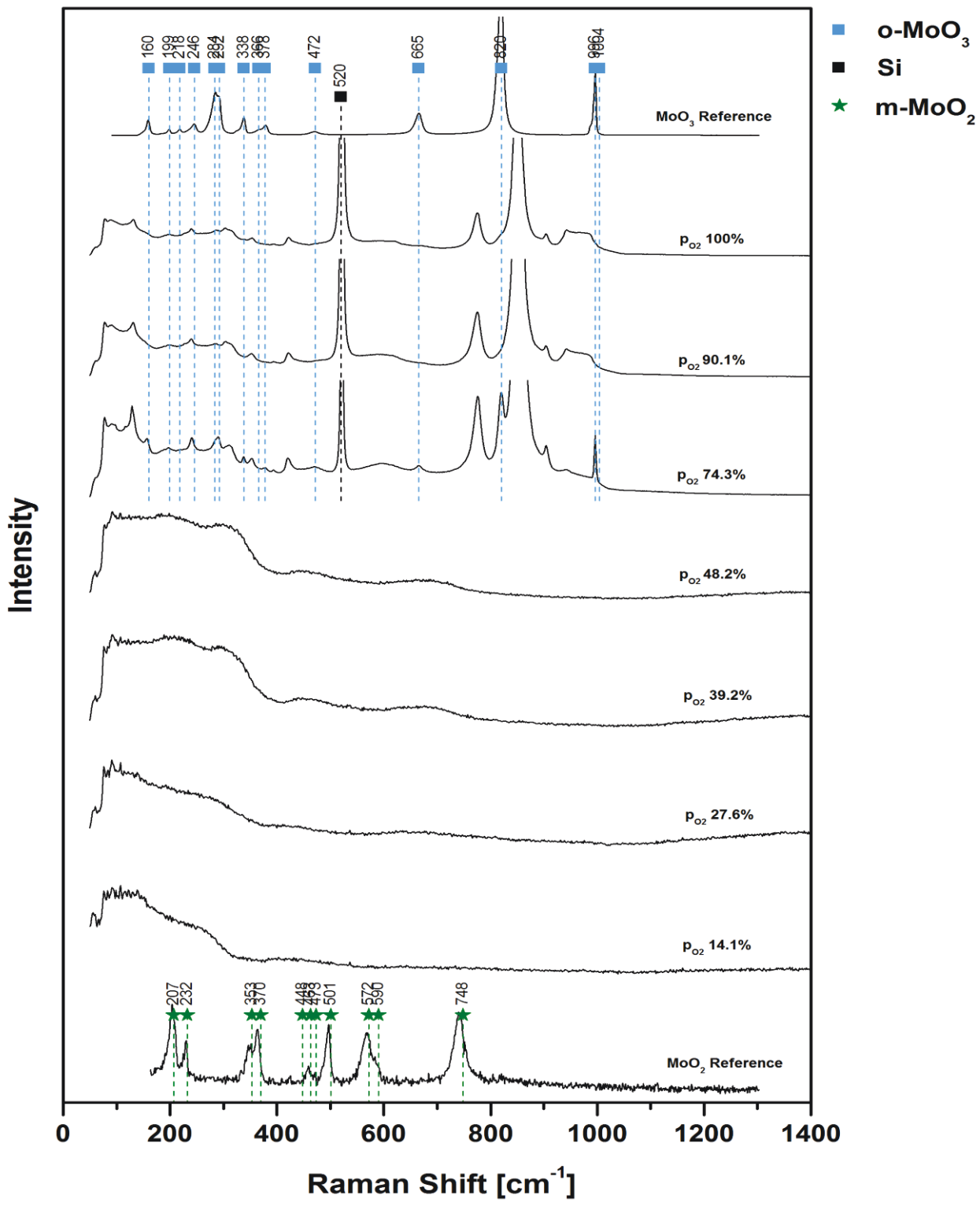

Figure 4.2: Raman spectra of the reactively sputtered films deposited on silicon. MoO_2 and MoO_3 reference data curves are added from the *RRUFF database* for comparison (λ = 532 nm) [65, 66]. The peak positions are according to *Blume* [44].

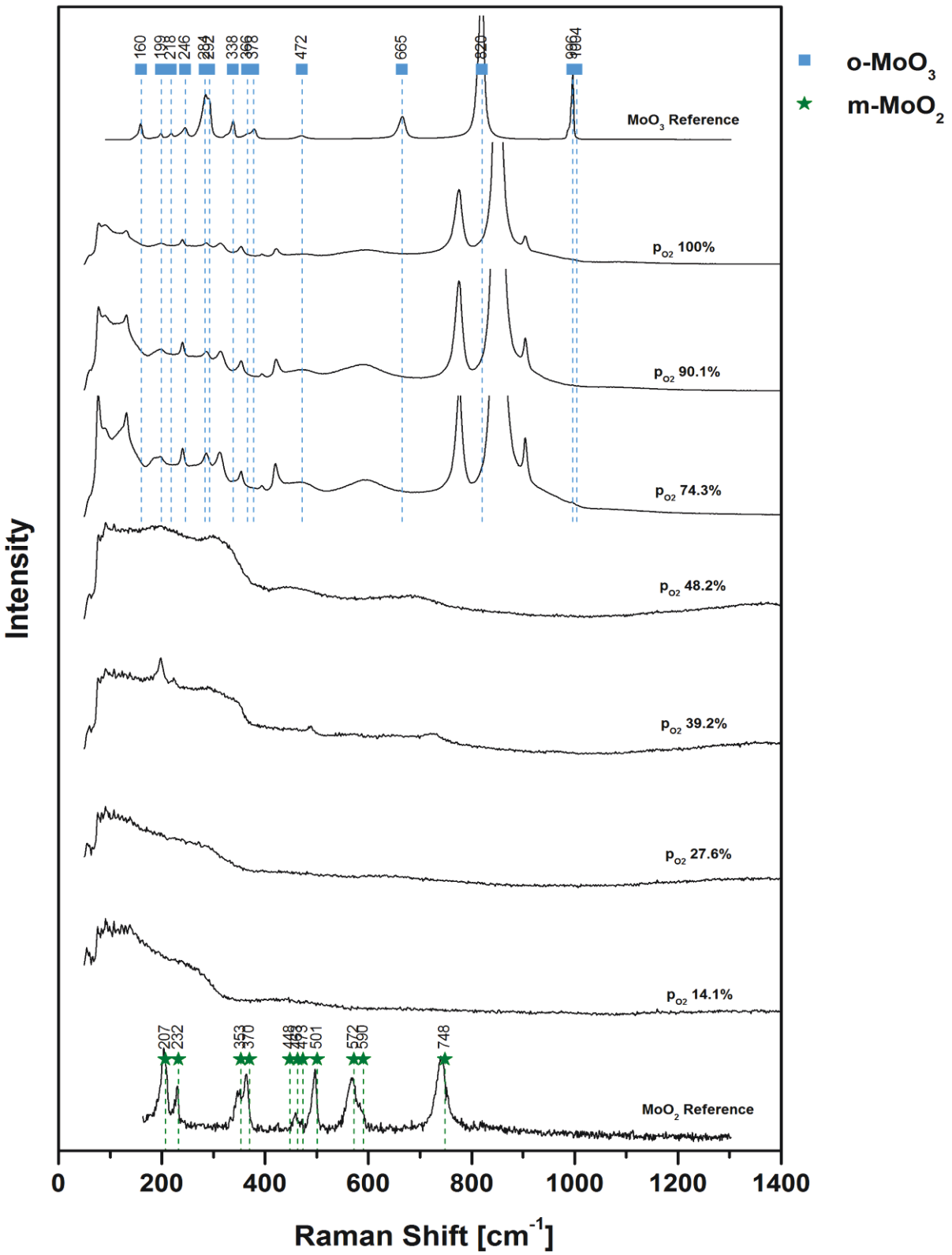

Figure 4.3: Raman spectra of the reactively sputtered films deposited on glass. MoO_2 and MoO_3 reference data curves are added from the *RRUFF database* for comparison (λ = 532 nm) [65, 66]. The peak positions are according to *Blume* [44].

The Raman spectra obtained from the films sputtered using the compound targets are shown in Figure 4.4. They are compared with the film sputtered reactively with p_{O2} = 48.2%. Similar to their reactively sputtered equivalent, the MoO_2 and MoO_x target films also show very broad peaks impeding an unambiguous phase identification based on the Raman spectra. The Raman signals do not show any specific observable difference between silicon and glass substrates.

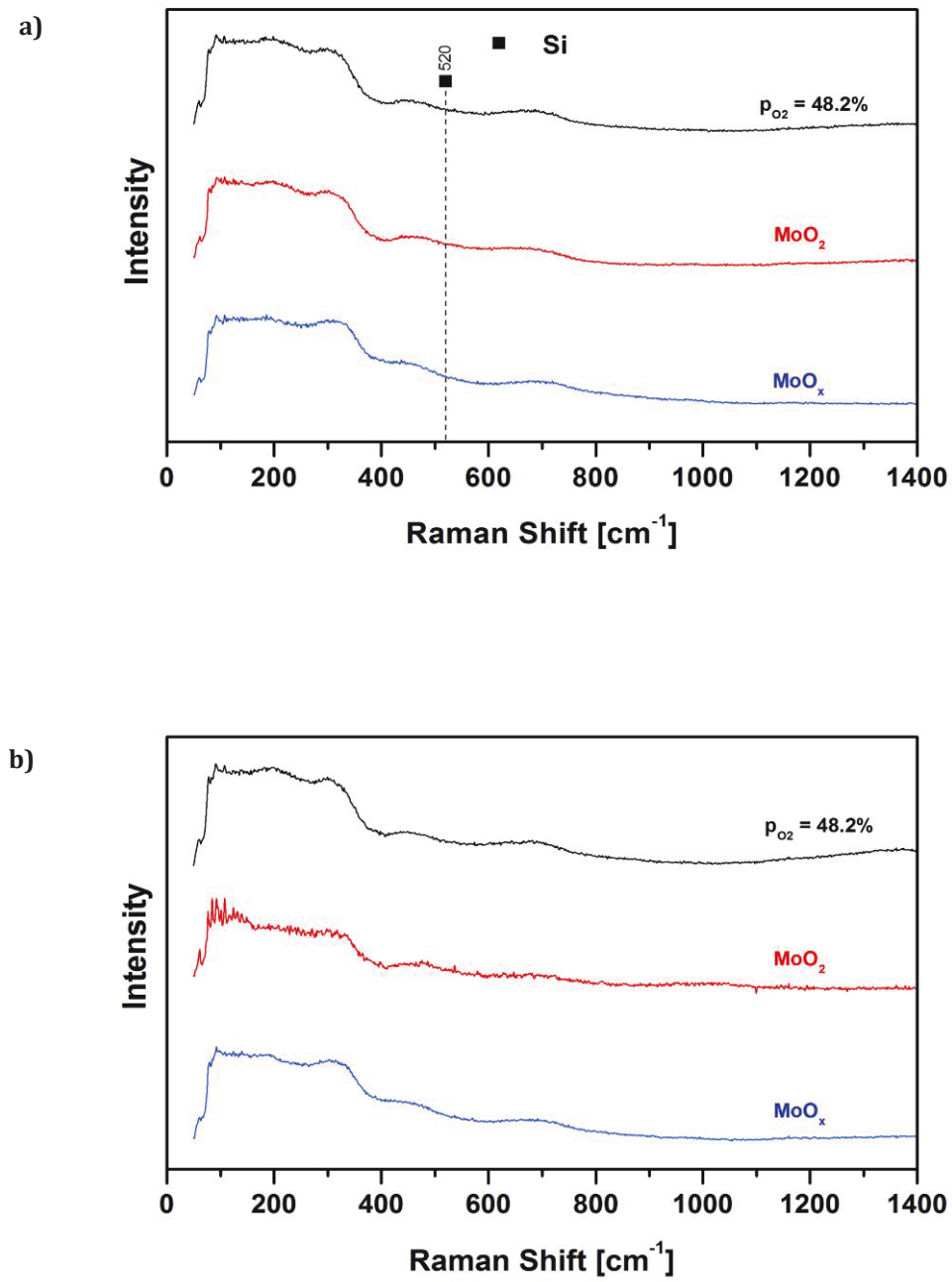

Figure 4.4: Raman spectra of the film **reactively sputtered** with p_{O2} = 48.2% (**black** line) in comparison with the films grown from the MoO_2 (red line) and MoO_x targets (blue line) deposited on a) silicon and b) glass substrates.

4.3 Microstructure

In general, the films deposited on silicon (see Figure 4.5), reveal a higher grade of crystallinity than those deposited on glass (see Figure 4.6). Since all specimens were synthesised with equal process conditions, there is apparently an influence of the substrate on the crystallinity of the grown films. The substrate influence on the crystallinity can be explained by the difference in crystallinity and free surface energies of both substrates. This could lead to different adsorption conditions for the adatoms, which in turn leads to different growth conditions of the crystals in the early stages of film formation determining the subsequent competitive growth. In addition, silicon is more electrically conductive than glass and, thus, the bias voltage causes a higher ion current and so nucleation is fostered on silicon substrates.

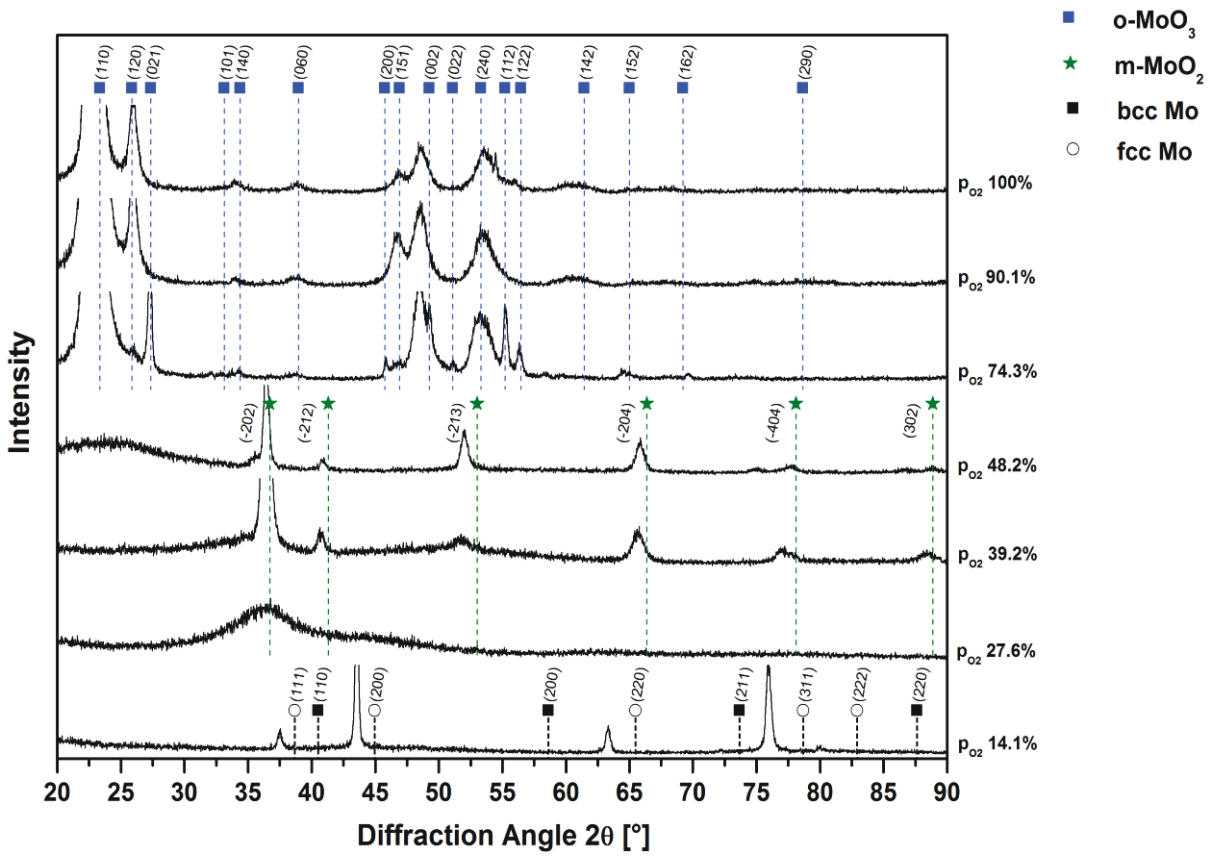

Figure 4.5: XRD diffractograms of the reactively sputtered films deposited on silicon at different oxygen partial pressures.

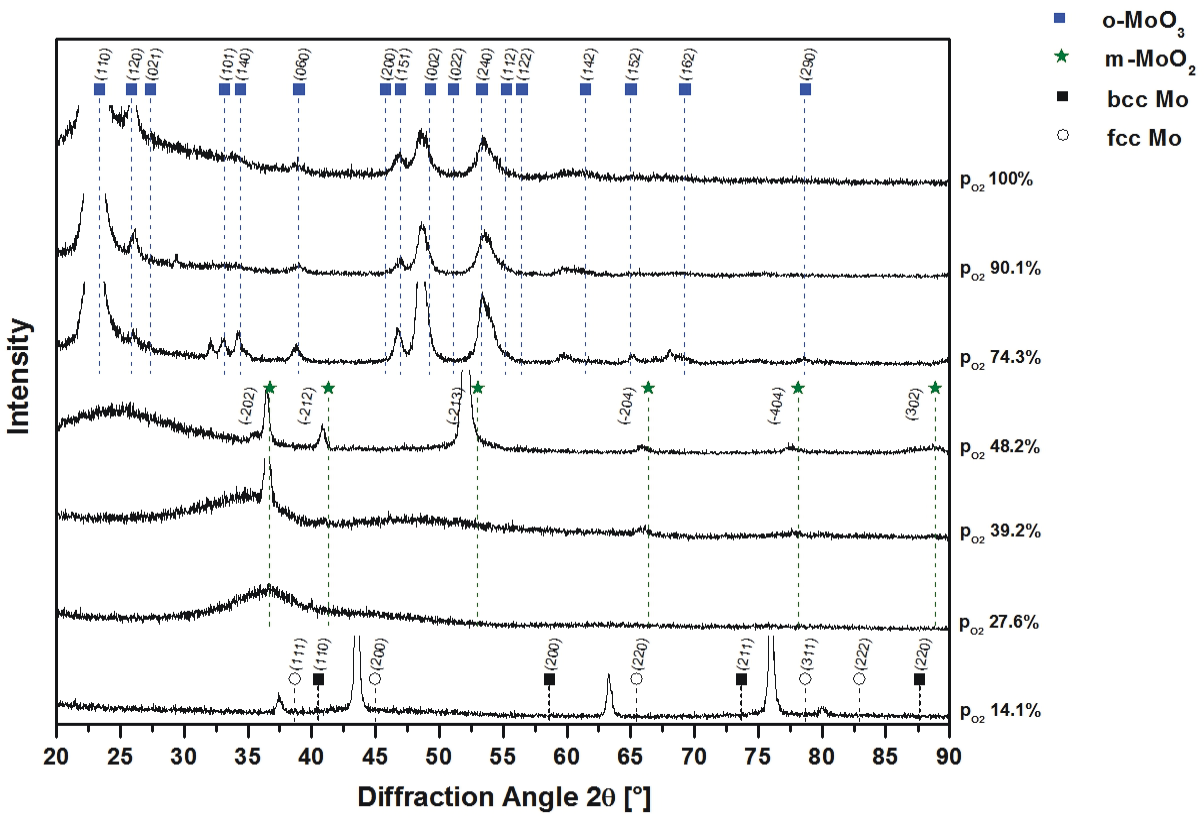

Figure 4.6: XRD diffractograms of the reactively sputtered films deposited on glass at different oxygen partial pressures.

Starting with the film that contains the lowest amount of oxygen, p_{O2} = 14.1%, there are five peaks recognisable which may be correlated to the Mo phase. It has been shown by *Kendig et al.* that sputter deposited nanoscale Mo films can exhibit huge 2θ shifts (exceeding 10°) by incorporation of oxygen and hydrocarbon impurities at interstitials or grain boundaries, which leads to an expansion of the Mo lattice [67]. *Faou et al.* have also reported the occurrence of Mo in reactively sputter deposited Mo films with an O_2 gas flow of 2 sccm exhibiting a 2θ shift [68]. In the present thesis, the oxygen partial pressure p_{O2} = 14.1% is associated with an oxygen flow rate of 2.5 sccm O_2. It is evident that a direct comparison is not possible due to differences in the design of the deposition systems, but it highlights that the presence of an oxygen containing Mo phase is possible within these process parameters. By comparing the measured data with the body-centred cubic (bcc) Mo reference pattern [69], it can be seen that apparently a peak shift has taken place which is inhomogeneous with respect to the reference pattern positions. As a consequence, the lattice constant *a* has been calculated by using equation (4) (see section 3.2.3) and the results are shown in Table 4.2.

Table 4.2: Calculated lattice constant *a* of the bcc-Mo phase based on the diffraction angles 2θ from Figure 4.5 (p_{O2} = 14.1%).

2θ	θ	$\sin^2(\theta)$	(hkl)	$h^2+k^2+l^2$	$\lambda^2/(4a^2)$	a [Å]
37.5	18.75	0.10332333	110	2	0.05166166	3.38771234
43.5	21.75	0.13731281	200	4	0.0343282	4.15590093
63.3	31.65	0.2753405	211	6	0.04589008	3.59444052
75.9	37.95	0.37819249	220	8	0.04727406	3.54143493
80	40	0.41317591	310	10	0.04131759	3.78811564

Bcc-Mo normally exhibits a lattice constant *a* of 3.147 Å [37], but since there are differences to the calculated constants shown in Table 4.2, the Mo lattice seems to be expanded. This may be explained by the incorporation of oxygen atoms into the Mo lattice as described previously. In addition, a face-centred cubic (fcc) Mo pattern published in [70] was also compared to the measured data which shows a consistent peak shift in relation to the measured peak positions (see Table 4.3). This Mo modification is a hypothetical one whose existence was not proven yet [70]. It is based on *ab initio* calculations for 3d, 4d and 5d transition metal carbides and nitrides by *Häglund et al.*, who investigated the electron structure of metal carbides and nitrides (NaCl structure type e.g. MC, MN) as well as other complex compounds, e.g. M_3C or M_7C_3 [71].

Table 4.3: Calculated lattice constant *a* of the fcc-Mo phase based on the diffraction angles 2θ from Figure 4.5 (p_{O2} = 14.1%).

2θ	θ	$\sin^2(\theta)$	(hkl)	$h^2+k^2+l^2$	$\lambda^2/(4a^2)$	a [Å]
37.5	18.75	0.10332333	111	3	0.03444111	4.14908331
43.5	21.75	0.13731281	200	4	0.0343282	4.15590093
63.3	31.65	0.2753405	220	8	0.03441756	4.1505024
75.9	37.95	0.37819249	311	11	0.03438114	4.15270055
80	40	0.41317591	222	12	0.03443133	4.14967277

According to the reference pattern [70], the lattice constant of the fcc modification is 4.03 Å. This value is lower than the one calculated in Table 4.3, but the fact that the latter is constant, strongly points towards the presence of an fcc phase. However, it needs to be kept in mind that the fcc-Mo has not yet been experimentally verified. In summary, the present data appears to be inconclusive with respect to the nature of the film deposited with p_{O2} = 14.1% and further investigations are necessary.

The three XRD diffractograms of the film grown with p_{O2} = 27.6%, 39.2% and 48.2% show similarities. The film sputtered with p_{O2} = 27.6% is essentially amorphous, but a gradual formation of a crystalline structure seems to take place with increasing O_2 partial

pressure. The XRD signals of those films seem to originate from the m-MoO_2 (monoclinic) phase. A comparison with the MoO_2 reference pattern [72] shows that this pattern is stringent and that obviously a peak shift has taken place as well.

The next three diffractograms from the films synthesised with p_{O2} = 74.3%, 90.1% and 100% may stem from the o-MoO_3 phase, because they are in good agreement with the reference pattern [73]. On silicon, the film with p_{O2} = 74.3% reveals several peaks that do not occur in the two succeeding films, which are the (021), (200), (022), (112) and (122) peaks. This could be explained by the fact that the last two films are much thinner than the film grown with p_{O2} = 74.3% and, thus, they seem to be less crystalline. It has to be mentioned here that for those three films the dominant peak is the (110) peak at ~23°. In the diffractograms, it has been cut off so that the other peaks are still visible.

It was already shown in section 4.1 that the films sputtered from the MoO_2 and MoO_x targets have almost identical molybdenum and oxygen concentrations compared to the films sputtered reactively with p_{O2} = 39.2% and 48.2%. Figure 4.7 illustrates that also the XRD diffractograms of those films look very similar. Since the film with p_{O2} = 48.2% revealed the same m-MoO_2 phase as the film grown with p_{O2} = 39.2%, but a more developed one, this film is presented in Figure 4.7. According to the measured XRD data, the films sputtered from the compound targets also consist of m-MoO_2. The diffractogram of the film sputtered from the MoO_2 target contains an additional peak at ~35°. This peak could also originate from the m-MoO_2 phase, because in the reference pattern there are several peaks present around 36°, separated by only ~0.1° each. Since a peak shift has presumably taken place for those films too, it is therefore possible that the peak at ~35° originates from m-MoO_2 as well. Comparing the XRD diffractograms of the specimens grown on silicon and glass (see Figure 4.7a and b), they seem to have a similar grade of crystallinity, which is also reasonable when keeping in mind that no bias and no heating was applied to the substrates of the films synthesised non-reactively.

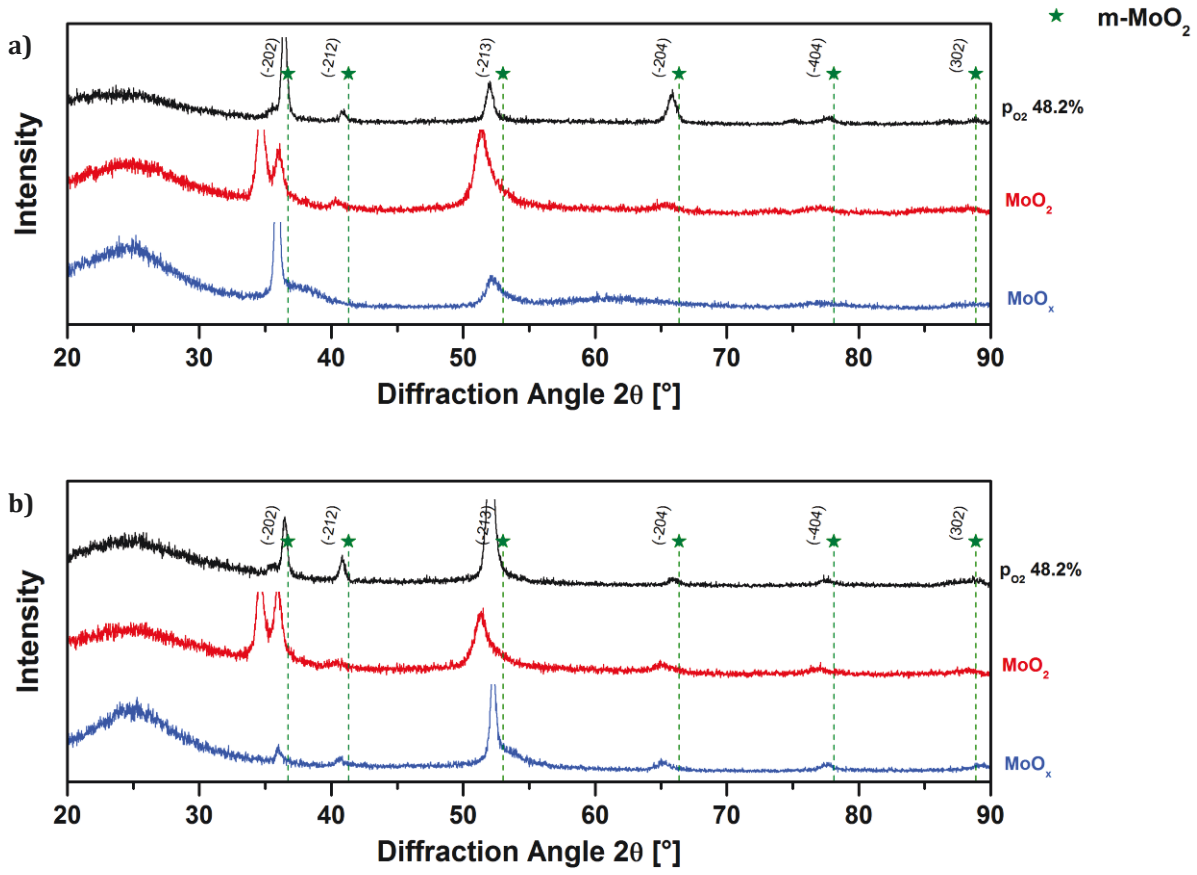

Figure 4.7: XRD diffractograms of the film **reactively sputtered** with p_{O2} = 48.2% (**black** line) in comparison with the films grown from the MoO_2 (red line) and MoO_x targets (blue line) deposited on a) silicon and b) glass substrates.

4.4 Morphology

The secondary electron SEM images of the reactively deposited films are shown in Figure 4.8. In the top view image of the film deposited with p_{O2} = 14.1% (see Figure 4.8a), there are very bright grains noticeable. Those grains are nanocrystalline and approximately 100 nm in diameter. Based on the previously discussed XRD diffractogram, those grains can be assigned to the polycrystalline Mo phase. The cross section reveals a very narrow columnar structure with a graded substrate-film interface. It has been reported by *Faou et al.* that such a graded interface can origin from the oxygen atoms which hinder the molybdenum adatoms' mobility, thus, influencing the competitive growth of the crystals [68].

The film with p_{O2} = 27.6% (see Figure 4.8b) is essentially amorphous according to XRD measurements. From the topography and the cross section of that film, it also looks like no crystalline phase has been formed as no columns or grains are visible. This might be interpreted that there is a transition from one phase to another and that under these conditions (oxygen partial pressure, temperature) no crystalline structure could be formed.

In the top view of the film with p_{O2} = 39.2% (see Figure 4.8c) it seems that islands have been formed, some of which grew together to bigger clusters. There is also a columnar structure observable in the cross section which has been developed by competitive growth. In addition to the corresponding XRD diffractogram, the SEM pictures of that film could be interpreted as the onset of the formation of the MoO_2 phase.

The surface micrograph of the film with p_{O2} = 48.2% (see Figure 4.8d) indicates the formation of crystals which are aligned in a dense columnar structure, as evidenced by the cross section image. According to the interpretation of the XRD patterns of that film, this might be an indication for the formation of the polycrystalline m-MoO_2 phase.

The top view of the film with p_{O2} = 74.3% (see Figure 4.8e) reveals the existence of crystals of different shape. Some are apparently horizontally aligned to the surface and appear flat and flaky, while others are needle-like grown out of the surface. By taking a closer look at those needles, they seem to consist of bundles of flat crystals which have grown in different directions. The cross section image shows a columnar structure and a rough specimen surface due to the vertically oriented crystals.

The last two films with p_{O2} = 90.1% and 100% (see Figure 4.8f and g) obviously exhibit a similar morphology. The grains are flat and flaky and oriented parallel to the surface like parts of the grains in the previously described film with p_{O2} = 74.3%. Their cross section images evidence dense columnar structures as well. The occurrence of such flat and flaky-like crystals has also been reported by *Fateh et al.* for DC reactively sputtered V_2O_5 films deposited on silicon [74]. The similarity of the crystallographic and chemical properties between MoO_3 and V_2O_5 has been reported in literature [75-77]. The relation between

both oxides is emphasised by the remarkable solubility of MoO_3 in V_2O_5. [75, 76]. Further, the high pressure β-modification of V_2O_5 (monoclinic or tetragonal) is composed of distorted VO_6 octahedra that also form zig-zag chains leading to a layered structure similar to α–MoO_3 [77]. Therefore, it is possible that both oxides exhibit similar morphology. Since the horizontally aligned flaky crystals of those films can be identified as the o-MoO_3 phase, further conclusions are possible for the needle-shaped crystals in the previously discussed film grown with p_{O2} = 74.3%. It was shown in the XRD diffractogram of that film, that there are several additional peaks, implying additional crystal orientations, which can also be related to the o-MoO_3 phase (see section 4.3). Thus, those needle-like crystals in p_{O2} = 74.3% can also be o-MoO_3 crystals of different orientation, which are missing in the films with p_{O2} = 90.1% and 100% because of a lack of competitive growth due to a reduced sputter yield caused by target poisoning (see section 4.1).

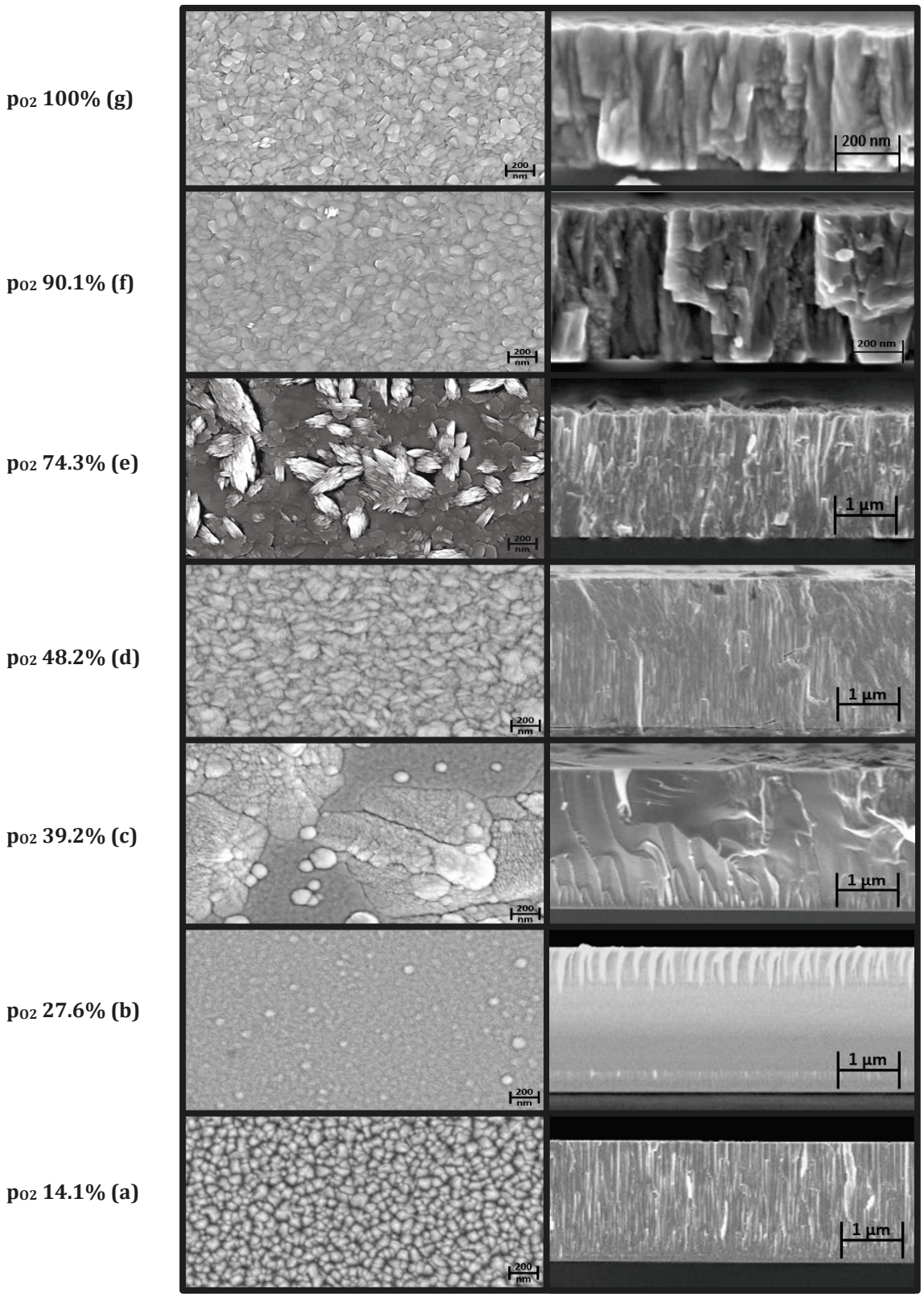

Figure 4.8: The morphology of the reactively sputtered films according to their secondary electron SEM images. Topography on the left, cross section on the right side. The pictures are in order of increasing oxygen partial pressure from bottom to top.

The top view secondary electron SEM images of both films sputtered from the compound targets are blurry as shown in Figure 4.9. This might be explained by a low electrical conductivity and, hence, charging effects during image recording. The film sputtered from the MoO_x target exhibits a dense columnar structure as illustrated in the cross section image. The film synthesised using the MoO_2 target on the other hand, seems to have a columnar structure in the early growth stage, but at about 50% of the thickness it has been interrupted by re-nucleation. It is possible that at 50% of the thickness, the density of defects is that high that they serve as new nucleation sites by further incoming atoms.

MoO_2 target

MoO_x target

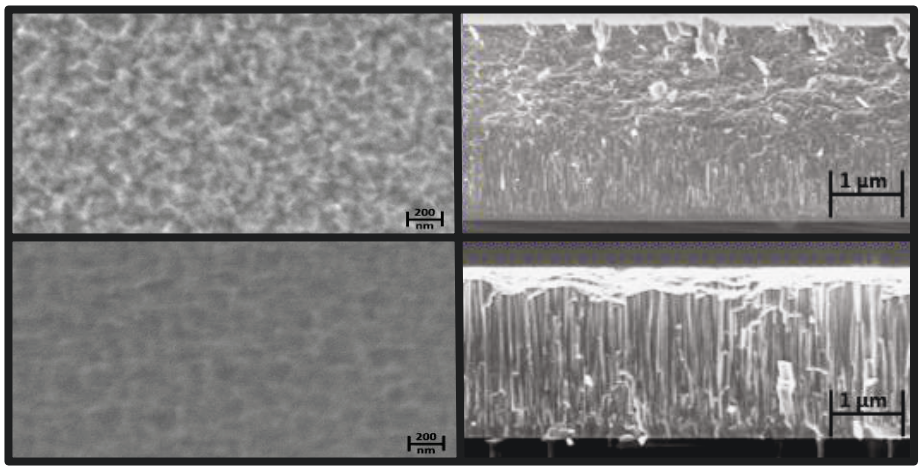

Figure 4.9: Comparison of the secondary electron SEM images of the films grown from the MoO_2 (top) and MoO_x (bottom) targets. Topography on the left, cross section on the right side.

4.5 Optical Appearance

In order to describe the optical appearance, photos of the films grown on glass substrates were taken by using a digital camera (see Figure 4.10). Starting from the bottom, the first four specimens with p_{O2} equal to 14.1%, 27.6%, 39.2% and 48.2% look similar. They appear black or greyish and are opaque. The third one with p_{O2} = 39.2%, is more grey than the other three. The last three films of the series with p_{O2} = 74.3%, 90.1% and 100% appear yellowish and transparent. At the edges of the samples, there is further a slight greenish colouration recognisable as well. The film grown with p_{O2} = 74.3% is darker than the other two.

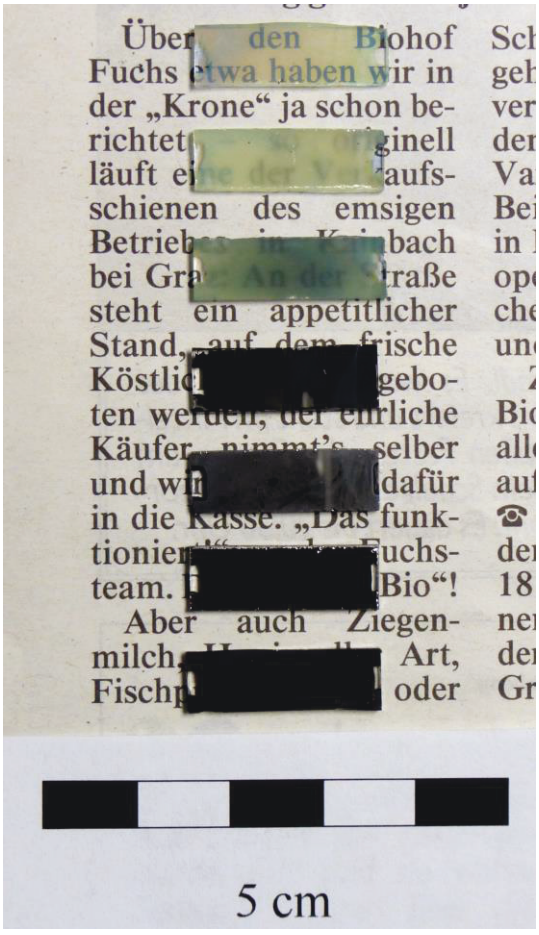

p_{O2} 100%, 0.2 µm

p_{O2} 90.1%, 0.8 µm

p_{O2} 74.3%, 2.2 µm

p_{O2} 48.2%, 2.7 µm

p_{O2} 39.2%, 2.7 µm

p_{O2} 27.6%, 2.3 µm

p_{O2} 14.1%, 1.9 µm

Figure 4.10: Photos of the reactively sputtered films in order of increasing oxygen partial pressure from bottom to top. The film thickness of each specimen is provided.

Apparently, a gradual change in optical properties can be observed by increasing the oxygen partial pressure, as it is shown in Figure 4.10. It seems that an oxygen partial pressure of 74.3% is a threshold because at this and higher pressures, the colour and transparency change. According to Table 4.1, an oxygen partial pressure of 74.3% is equivalent to an oxygen flow rate of 20 sccm, which in turn corresponds to an oxygen to argon flow ratio of 1:1.

The optical appearance can be related to the phases that were identified when analysing the XRD diffractograms and Raman spectra. The film with p_{O2} = 14.1% is metallic dark and opaque, which is in agreement with the Mo phase that is most likely present in the film. The gradual formation of the MoO_2 phase in the subsequent films with increasing oxygen partial pressure (p_{O2} = 27.6%, 39.2% and 48.2%) should lead to a reddish-brown, reddish-purple colouring [6, 7]. It is therefore possible that those films have a high density of defects altering their optical appearance. The yellowish colouration and transparent character of the films with p_{O2} = 74.3%, 90.1% and 100%, is due to the presence of the MoO_3 phase [34, 44], which was observed in the XRD diffractograms and Raman spectra. The slightly darker appearance of the film with p_{O2} = 74.3% may derive from its higher thickness (t_c = 2.2 µm) leading to enhanced light scattering as compared to the thinner films with p_{O2} = 90.1% (t_c = 0.8 µm) and 100% (t_c = 0.2 µm).

In Figure 4.11, the optical appearance of the films sputtered from the compound targets is visualised. Both films are black and opaque. Similar to the film sputtered reactively with p_{O2} = 48.2%, those films exhibit the m-MoO_2 phase according to their XRD patterns. The different colour with respect to MoO_2 may again be explained by a high density of defects. The film synthesised using the MoO_2 target shows weak adherence on the glass substrate and appears therefore inhomogeneous and partially chipped off.

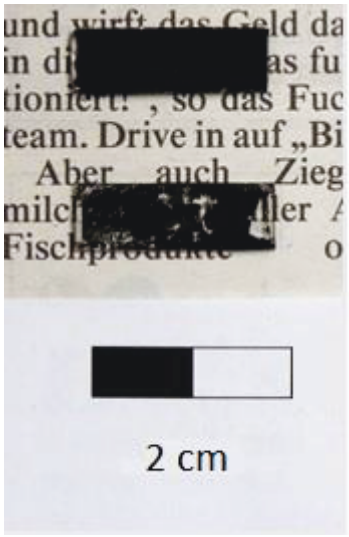

MoO_x, 2.6 µm

MoO_2, 2.1 µm

Figure 4.11: Comparison of the optical appearance of films sputtered from the MoO_x (top) and MoO_2 (bottom) targets on glass substrates. The film thickness of each specimen is provided.

4.6 Electrical Resistivity

The electrical resistivity of the four films of the reactively sputtered series shown in Figure 4.12 lies between 4.4×10^{-4} Ωcm and 1.3×10^{-3} Ωcm. The measured resistivity values are basically identical for both substrates, silicon and glass, indicating that the electrical measurements were not influenced by the substrate material. The films sputtered at oxygen partial pressures higher than p_{O2} = 48.2% are not illustrated, because electrostatic charging effects during measurement due to their insulating nature inhibited the determination of reliable values for their resistivity. This behaviour is related to the occurrence of the insulating o-MoO_3 phase as it was shown in the XRD diffractograms and Raman spectra. Both possible MoO_3 modifications have resistivities ranging from 10^7 to 10^{10} Ωcm and are insulating [34]. The other films reactively sputtered between p_{O2} = 14.1% and 48.2% vary only slightly in their resistivity. Apparently, there is an increase in resistivity up to p_{O2} = 39.2% followed by a slight decrease towards p_{O2} = 48.2%. The increase may be explained by the amorphous nature of those films and the decrease by the development of the MoO_2 structure. There is a difference in resistivity by two orders of magnitude between the film sputtered reactively with p_{O2} = 14.1% of potential metallic Mo phase composition and the value of Mo after [37]. This may be explained by the incorporation of oxygen into the molybdenum lattice hindering the electron motion and, hence, increasing the resistivity of the film.

The films grown by sputtering of the compound targets show similar resistivity values, which lie within the range of the reactively sputtered films.

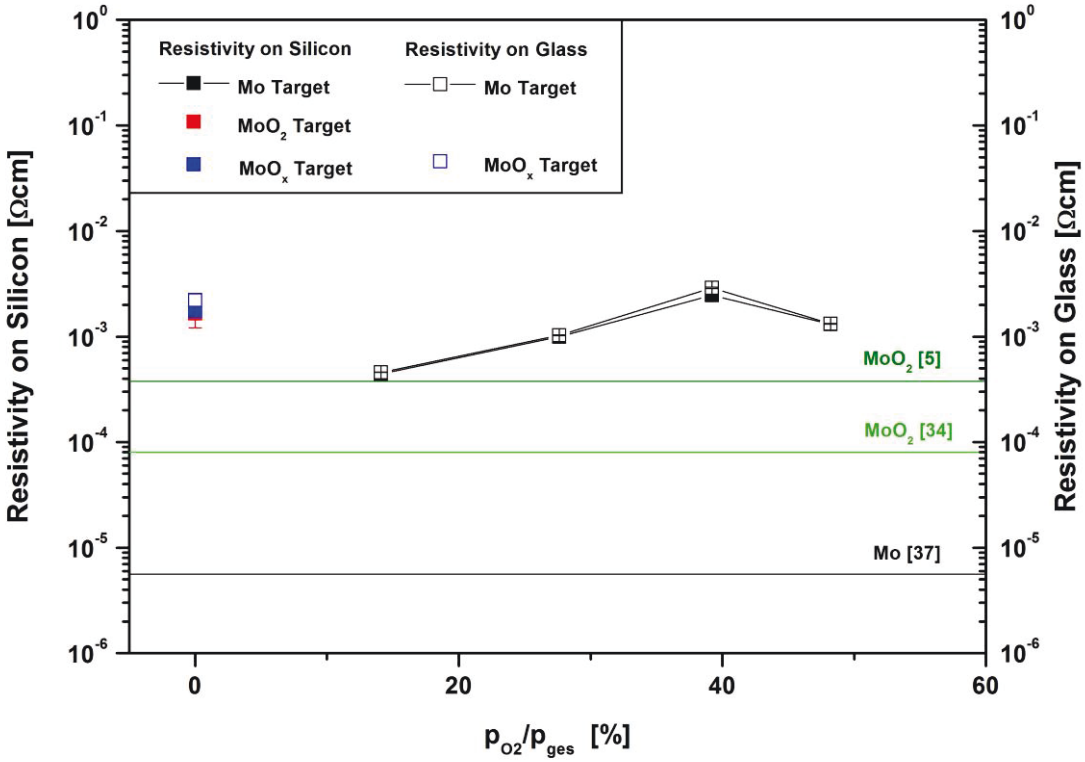

Figure 4.12: Electrical resistivity of the molybdenum oxide films deposited on silicon and glass substrates versus the oxygen partial pressure. The film grown by non-reactive sputtering from the MoO_2 target deposited on glass is not included since it was partially chipped off. As a guideline, values from literature are added for Mo [37] and MoO_2 [5, 34].

4.7 Mechanical Properties

All films exhibit compressive residual stress (see Figure 4.13), as it is typical for films grown under ion irradiation because the incoming ions/atoms induce lattice defects and film densification [78]. This peening effect is due to incoming particles exhibiting high kinetic energy, which is a function of the sputtering gas pressure as well as the substrate bias [78]. The film sputtered from the MoO_2 target has the highest compressive stress level. The film surpasses the stress level of the specimen grown from the MoO_x target by ~800 MPa and the most compressively stressed film of the reactively sputtered series, sputtered with p_{O2} = 48.2%, by ~600 MPa.

In comparison, the stress value obtained for the lowest oxygen partial pressure of the reactively sputtered films is about –550 MPa. This stress level can be explained by the incorporation of oxygen at lattice defects, such as interstitials and grain boundaries. It was already pointed out that this behaviour has been reported for molybdenum thin films, where oxygen and hydrocarbon impurities were incorporated into those lattice defects. This resulted in the expansion of the molybdenum lattice which in turn was responsible for the compressive stress [67]. The subsequent increase in stress with increasing oxygen partial pressure can be correlated with the gradual formation of the m-MoO_2 phase. The high compressive stress suggests a high density of defects in those films as it was already discussed with respect to their optical appearance. The film sputtered with p_{O2} = 74.3% is almost free of stress. This can be explained by the formation of the stable crystalline o-MoO_3 phase. A high grade of crystallinity is achieved and the lattice is relaxed, as evidenced by the measured low stress. The main reason for the subsequent increase in stress is the fact that the last two films of the series are much thinner and so their residual stress is higher, as it was shown in [79]. The difference in the thermal expansion coefficient between substrate and the films can also influence the residual stress, since the films were deposited at 120°C and then cooled down to room temperature. The average thermal expansion coefficient for MoO_3 is reported to be 5.8×10^{-5} K^{-1} between 25 and 500°C [28] and for a MoO_2 thin film 4.5×10^{-6} K^{-1} between 100 and 600°C [28]. In comparison, Si has a thermal expansion coefficient of 2.6×10^{-6} K^{-1} at 300 K [80]. Based on these data, the expansion mismatch is greater for MoO_3 than for MoO_2 and, thus, the thermal influence should be greater for MoO_3. Generally, a higher thermal expansion coefficient of the film as compared to the substrate leads to tensile stress, which might explain the lower stress state of the films with dominating MoO_3 structure. However, several other factors influence the evolution of the stress state as well, e.g. grade of crystallinity, grain size, crystal orientation, and further investigations are needed to understand the residual stresses of the molybdenum oxide thin films in detail.

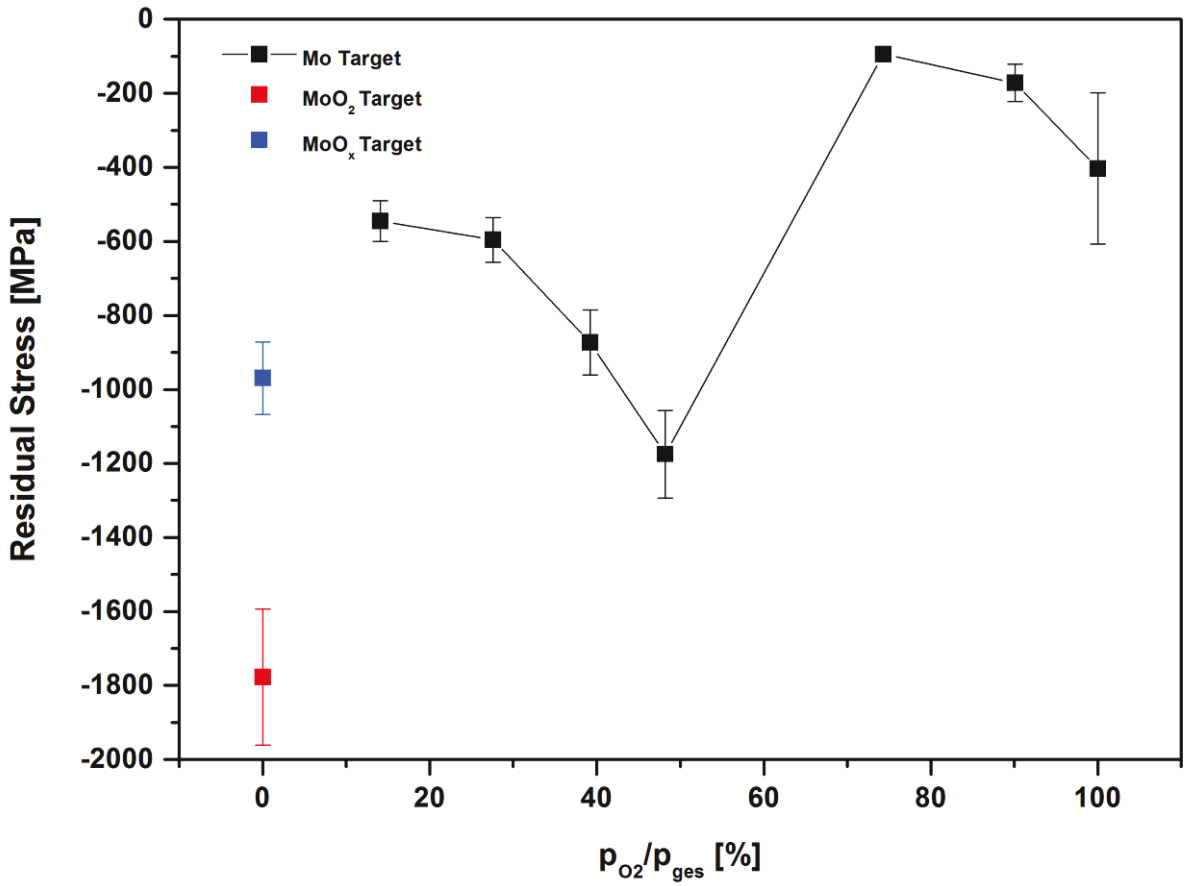

Figure 4.13: Residual stresses of the reactively as well as non-reactively sputtered films in relation to the oxygen partial pressure. An error of ±10% for the coating thickness determined by ball cratering and ±1 mm for the laser spot distance in the wafer curvature method was assumed for the calculation of the error bars.

In Figure 4.14, the results of the nanoindentation measurements are presented. Only films with a thickness ≥1 µm are illustrated because of the substrate influence on the mechanical properties at thinner films.

The film sputtered reactively with p_{O2} = 14.1% consists of Mo according to XRD interpretations, hence, the film is comparatively hard and stiff. The film sputtered with p_{O2} = 27.6% is essentially amorphous, thus this specimen is softer and less elastic than the previously described one. The gradual development of the m-MoO_2 structure in the reactively sputtered films with p_{O2} = 39.2% and 48.2% apparently causes an increase in hardness and Young's modulus. The huge decrease in mechanical properties for the film sputtered with p_{O2} = 74.3% can be related once more to the occurrence of the crystalline o-MoO_3 phase.

By taking a look at Figure 4.13, it can be seen that a correlation between residual stress and mechanical properties is present, but similar to Figure 4.13, the curve may mainly be

explained by the occurrence of the different phases and their grade of crystallinity. In general, films with dominating MoO_2 structure are harder and stiffer than films with MoO_3 structure.

The film sputtered from the MoO_2 target is harder and stiffer than the film synthesised using the MoO_x target (see Figure 4.14). However, both films reveal high values of hardness and Young's modulus, which is in agreement with their MoO_2 dominated structure.

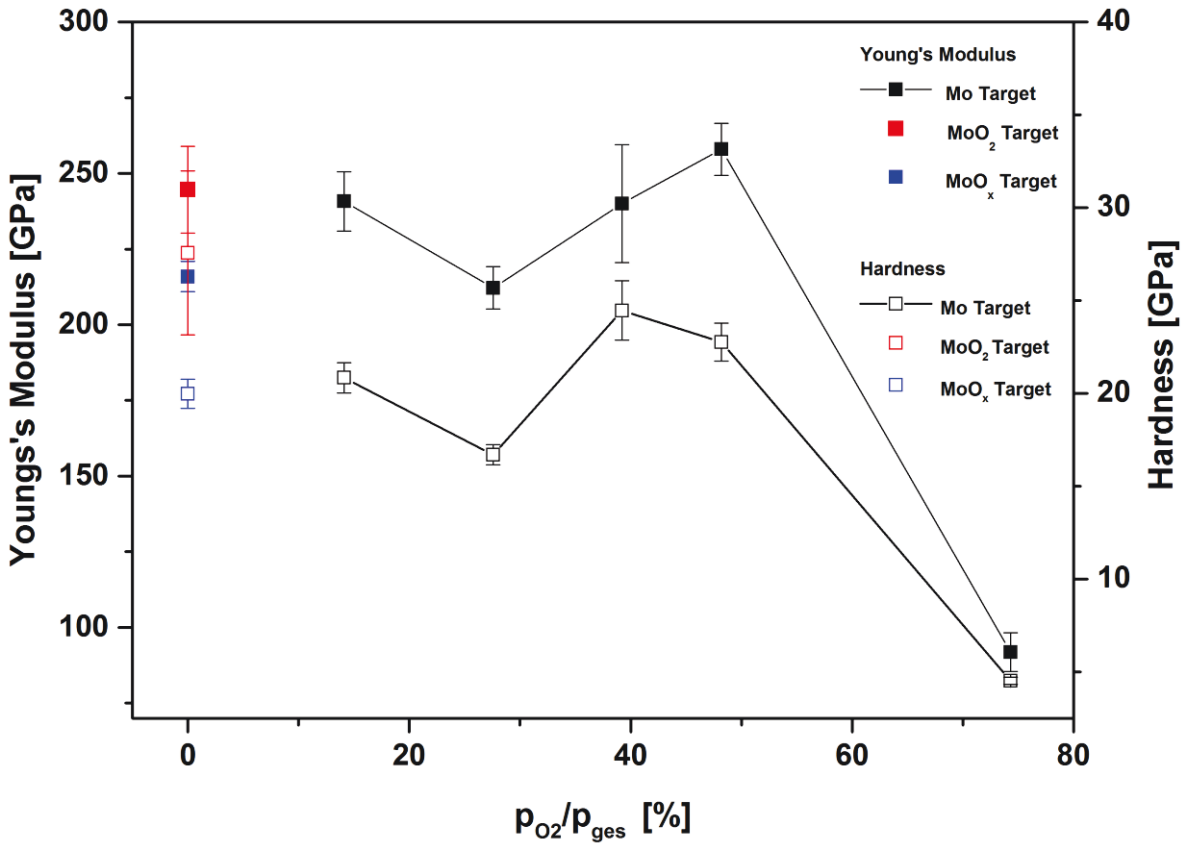

Figure 4.14: Young's modulus and hardness versus the oxygen partial pressure for the different molybdenum oxide films.

4.8 Films with reduced thickness

The influence of the film thickness on the previously discussed properties was studied as well, in particular for those films sputtered reactively with p_{O2} = 74.3%, 90.1% and 100% and the two films sputtered from the compound targets. The results of those thinner films exhibiting a thickness in the range of 100–200 nm are summarised in the following.

Starting with the EDS and WDS measurements as shown in Table 4.4, the chemical compositions of those thin films are in good agreement with their thicker equivalents (cf. Table 4.1). There are only differences for the WDS data of the films sputtered from the compound targets. The thinner ones seem to have ~30% more oxygen than the thicker films. Similar to the thicker films, the difference may be explained by adjusting the measurement voltage to the coating thickness. It is plausible that this adjustment is more important for thinner films, thus, the EDS concentrations are likely the more precise ones.

Table 4.4: Results of EDS, WDS and thickness measurements for the 100-200 nm thick films. The **reactively sputtered films** as well as the films from the MoO_2 and MoO_x compound targets are listed.

Deposition time [min]	O_2 Flow [sccm]	p_{O2}/p_{ges} [%]	Composition (EDS)		Composition (WDS)		Thickness [µm]
			Mo [at.%]	O [at.%]	Mo [at.%]	O [at.%]	
5.77	20	74.3	34	66	13	87	0.2
13.64	30	90.1	33	67	13	87	0.2
17.64	40	100	33	67	8	92	0.1
2	-	0	45	55	13	87	0.1
1.17	-	0	40	60	10	90	0.1

The XRD patterns of the reactively sputtered thin films are illustrated in Figure 4.15. There, the y-axis scale was altered compared to the XRD patterns in Figures 4.5 and 4.6 in order to visualise the change of intensities of the dominant (110) peak at ~23°. It is shown that the thinner films contain o-MoO_3, like their thicker equivalents, but they are less crystalline (see Figure 4.15). Their lower grade of crystallinity is related to the shorter deposition time and, thus, the formation of the crystalline MoO_3 phase is limited. The thin film with p_{O2} = 74.3% deposited on glass even seems to be completely amorphous. Apart from that exception, no difference in crystallinity is detectable for these films comparing silicon and glass substrates, because they are still in an early stage of film growth. This finding is contrary to the films deposited for 30 min, where a difference in crystallinity on both substrates was observed as a consequence of the already advanced competitive crystal growth (see section 4.3).

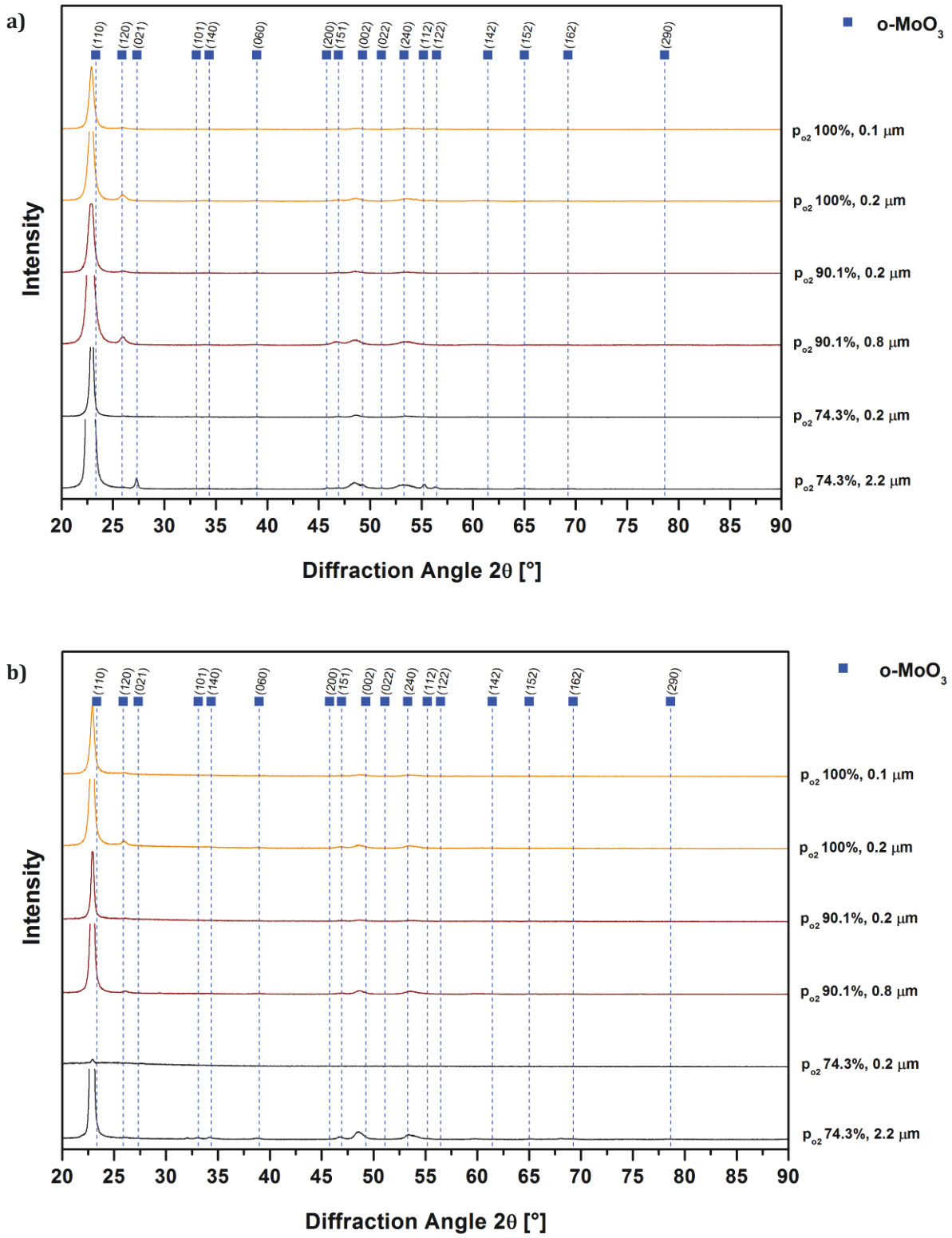

Figure 4.15: XRD diffractogramsof the reactively sputtered thin films with p_{O2} = 74.3%, 90.1% and 100% in comparison to their thicker equivalents deposited on a) silicon and b) glass substrates.

The compound target films are completely amorphous on both substrates according to their XRD patterns, as illustrated in Figure 4.16. Apparently, the substrate heating that was conducted for the reactively sputtered series has clearly fostered crystallisation as evidenced in the respective XRD diffractograms.

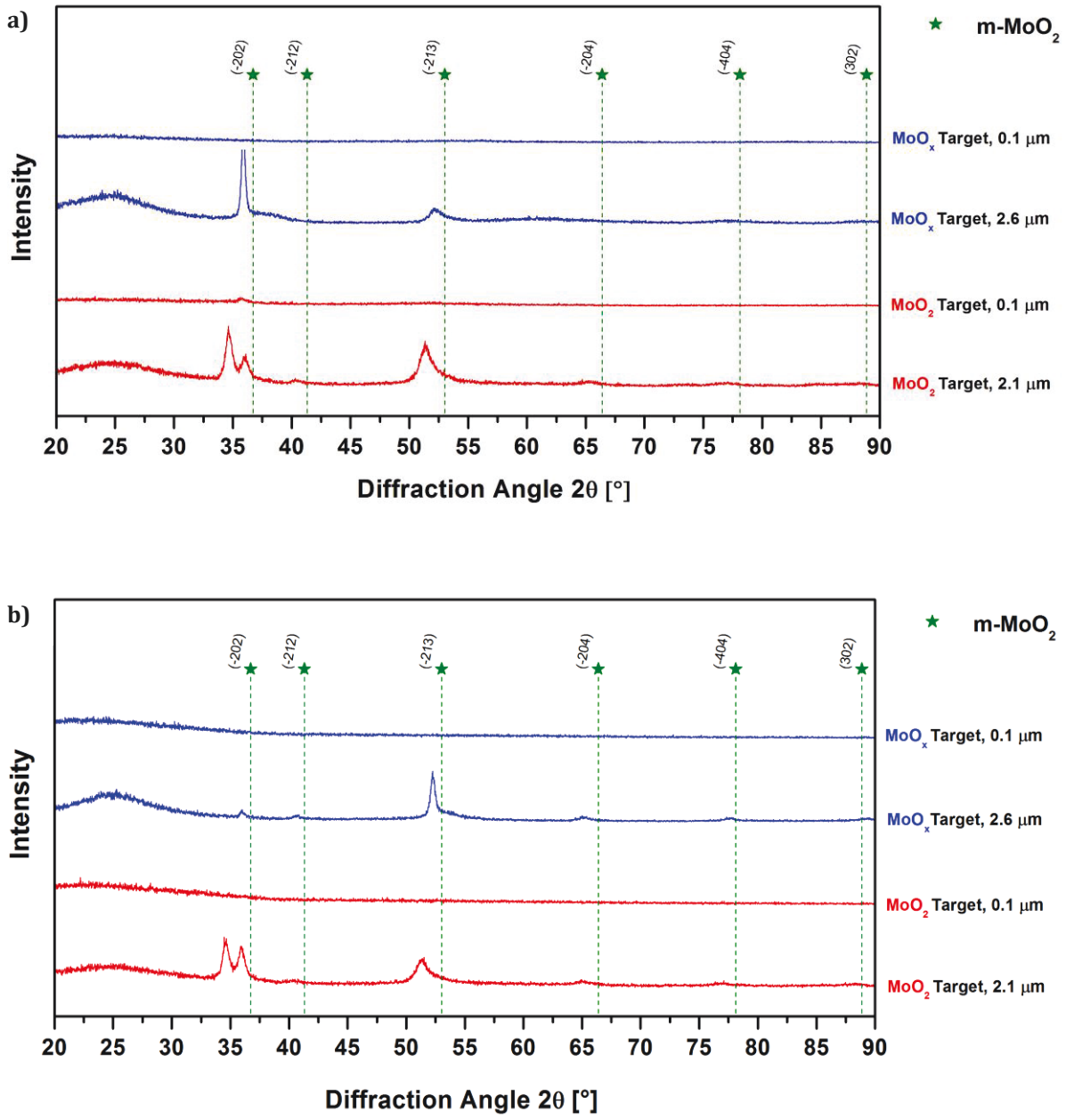

Figure 4.16: XRD diffractograms of the films grown from the MoO_2 (red line) and MoO_x targets (blue line) deposited on a) silicon and b) glass substrates.

No changes between the thicker and the thinner films were observed in the Raman spectra, regardless of whether the films were sputtered reactively or non-reactively.

The optical appearance of the reactively sputtered films is visualised in Figure 4.17. In general, it seems that all thinner films are more transparent than the thicker ones and that their colour has changed as well. The film deposited with p_{O2} = 74.3% appears bluish, like the subsequent one with p_{O2} = 90.1%. The film with p_{O2} = 100% has a yellow-greenish colour. The films grown from the compound targets remain very opaque and dark as shown in Figure 4.18. The thin film synthesised from the MoO_2 target exhibits a much better adherence on the glass substrate than its thicker equivalent.

Figure 4.17: Comparison of the optical appearance between the thicker (left) and thinner (right) films synthesised with p_{O2} = 74.3%, 90.1%, and 100%.

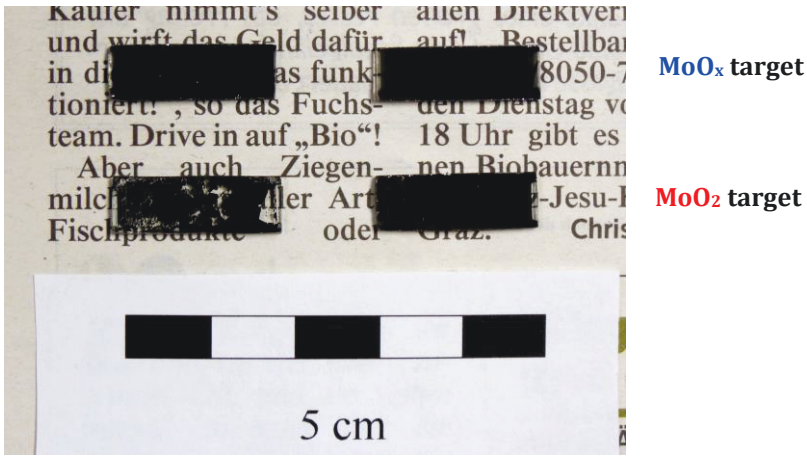

Figure 4.18: Comparison of the optical appearance between the thicker (left) and thinner (right) films grown from the MoO_x (top) and MoO_2 targets (bottom).

The morphology of the thinner reactively sputtered films can be described based on their secondary electron SEM images as shown in Figure 4.19. The topography and cross section images of the specimens with p_{O2} = 90.1% and 100% already show similar morphology and columnar structure in an early growth stage as their thicker equivalents, which are depicted in Figure 4.8. On the other hand, the morphology of the film with p_{O2} = 74.3% differs from its much thicker equivalent. The topography image shows planar zones with lamella packages in between, while the cross section image reveals a hardly developed and unspecific structure.

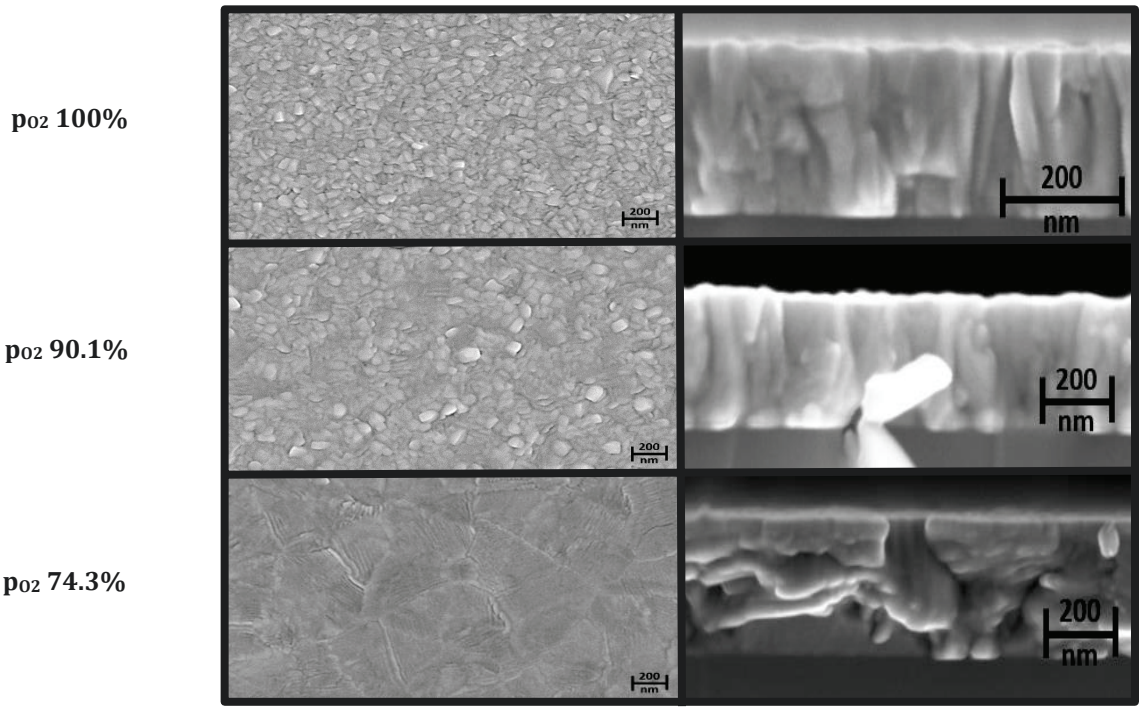

Figure 4.19: The morphology of the thinner reactively sputtered films according to their secondary electron SEM images. Topography on the left, cross section on the right side. The pictures are in order of increasing oxygen partial pressure from bottom to top.

The topography images of the thinner films synthesised from the compound targets reveal an early stage morphology of the MoO_2 target sputtered film as shown in Figure 4.20. Apparently, the structure lacks any long range order, as evidenced in the respective XRD diffractogram in Figure 4.16. The topography image of the film sputtered from the MoO_x target as well as the cross section images do not show any specific developed structure.

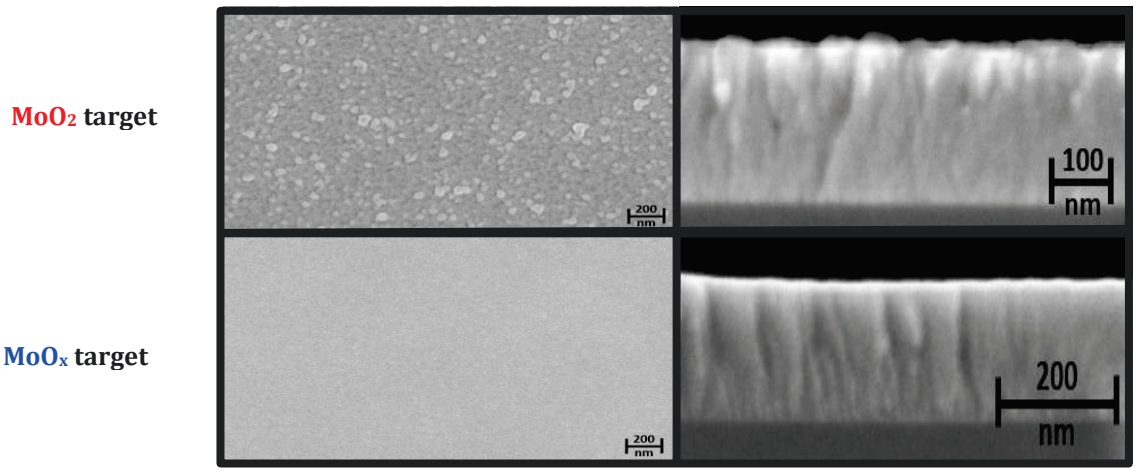

Figure 4.20: Comparison of the secondary electron SEM images of the thinner films grown from the MoO_2 (top) and MoO_x (bottom) targets. Topography on the left, cross section on the right side.

The results of the residual stress and electric resistivity measurements are listed in Table 4.5. No substrate influence on the electrical resistivity of the thinner films was detectable. Thus, only values from specimen grown on silicon are listed.

The thinner reactively sputtered films reveal slightly higher compressive stresses than their thicker equivalents, as it was expected. Since those films also seem to consist of o-MoO_3, they showed a dielectric behaviour as well.

Table 4.5: Comparison of residual stress and electrical resistivity values of the thicker and thinner films. The **reactively sputtered films** as well as the films grown from the MoO_2 and MoO_x compound targets are listed. The electrical resistivity values were obtained from the films deposited on the silicon substrate.

p_{O2}/p_{ges} [%]	Residual stress (thick film) [MPa]	Residual stress (thin film) [MPa]	El. Resistivity (thick fim) [Ωcm]	El. Resistivity (thin film) [Ωcm]
74,3	-94	-96	dielectric	dielectric
90,1	-172	-175	dielectric	dielectric
100	-403	-432	dielectric	dielectric
0	-1777	-1283	1.66×10^{-3}	1.67×10^{-3}
0	-969	-92	1.76×10^{-3}	1.62×10^{-2}

In contrast, the thinner compound target films reveal 500 MPa and 900 MPa less stress than the thicker ones. This may indicate that the density of defects in those films is much lower and perhaps their amorphousness also influences the stress value. The MoO_2 target thin film has an identical electrical resistivity as the thicker equivalent, whereas a difference of one order of magnitude is recognisable for the MoO_x target film. The reason may lie in the morphology of the films as shown in Figure 4.20. The MoO_x target film lacks

any developed structure in the early growth stage, which could result in an increase of the electrical resistivity.

5 SUMMARY AND OUTLOOK

5.1 Summary

Within this thesis, molybdenum oxide thin films with varying oxygen concentration were synthesised by reactive and non-reactive DC magnetron sputter deposition to study synthesis-structure-property relations in the system Mo-O. A general material characterisation was conducted including phase analysis by X-ray diffraction and Raman spectroscopy, chemical composition determination based on energy and wavelength dispersive X-ray spectroscopy as well as measurements of electrical resistivity and mechanical properties. In addition, scanning electron microscopy images were used to describe the obtained morphology.

First of all, it can be concluded that all investigated properties of the reactively sputtered molybdenum oxide thin films, i.e. optical, electrical and mechanical properties, are tuneable by varying the oxygen concentration. These properties are related to the occurring molybdenum and molybdenum oxide phases. Evaluation and interpretation of XRD diffractograms indicates the formation of an oxygen containing Mo phase, which is replaced by the monoclinic MoO_2 and eventually the orthorhombic MoO_3 phase with increasing oxygen partial pressure within the working gas. The Raman spectra confirm the presence of MoO_3 in the respective films. The films containing Mo or MoO_2 phases show similar electrical resistivity, independent of the substrate material. However, the films with dominating MoO_3 phase are insulating. The gradual formation of the MoO_2 phase correlates with a progressive increase in compressive stress, while the occurrence of MoO_3 leads to stress relaxation. A similar trend is observable for the Young's modulus and hardness, which evidences that specimens containing the MoO_2 phase are harder and stiffer than the specimens with MoO_3. The influence of the different phases is also reflected in the optical appearance of the films. The films with Mo or MoO_2 phases are dark and opaque, whereas MoO_3 dominated films are characterised by high transparency along with a yellowish colour. The progressive increase in oxygen partial pressure causes an increase in film thickness, but above p_{O2} = 48.2% target poisoning is evident resulting in reduced deposition rate. Concerning the morphology of the specimens, the secondary electron scanning electron microscopy images reveal dense columnar structures for all reactively sputtered films. The film sputtered with p_{O2} = 27.6% is the only exception lacking a developed morphology, but that film can be interpreted as the transition between the oxygen containing Mo and the MoO_2 phase leading to its essential featureless morphology.

The non-reactively sputtered films from the MoO_2 and MoO_x (with 50 mol% MoO_2 and 50 mol% MoO_3) targets show a dominating monoclinic MoO_2 phase according to XRD.

Their electrical resistivity values are very similar and in the same range as the values of the conductive reactively sputtered specimens. The film sputtered from the MoO_2 target is harder and stiffer and also has higher compressive residual stress than the film sputtered from the MoO_x target. Similar to the reactively sputtered films, the dominating MoO_2 structure in the films obtained from both compound targets leads to a dark and opaque optical appearance. The scanning electron microscopy images reveal a dense columnar structure for those films. For the non-reactively sputtered MoO_2 film, re-nucleation has taken place at ~50% of the coating thickness.

Decreasing film thickness lowers the grade of crystallinity for both reactively and non-reactively sputtered specimens. The influence is stronger on the films sputtered from the compound targets as they are completely amorphous. In contrast, the thinner reactively deposited specimens still reveal the dominant (110) peak of the orthorhombic MoO_3 phase. The benefit of substrate heating and substrate bias regarding crystallisation in the case of the reactively deposited films is evident. The transparency increases with decreasing film thickness, but the films synthesised using the MoO_2 and MoO_x targets still appear opaque and dark. The electrical resistivity is not influenced by the coating thickness, except of the film sputtered from the MoO_2 target. The residual stress measurements reveal ambiguous results. For the reactively sputtered films the stress level slightly increases, while the non-reactively obtained specimens show huge stress relaxation.

5.2 Outlook

In summary, the Mo-O system has the potential to present a promising alternative for currently used materials in TFT-LCDs. Taking a look at the obtained results, there are a few issues that need further clarification. The presence of an oxygen containing Mo phase within the reactively sputtered series seems plausible with respect to the interpreted X-ray diffractograms and the resulting material properties, but further investigations, such as X-ray photoelectron spectroscopy, may help clarifying the presence of such a phase. The mechanical properties need further investigations as well, since it is not clear how far the properties are actually related to the phases themselves, or rather to the densities of defects, crystal orientations or grades of crystallinity. In order to gain a better understanding of the films grown from the molybdenum oxide targets, it is evident that more deposition experiments are required. Within this thesis, only a first insight can be given to the non-reactively deposited films. Therefore, sputter deposition of a series of oxide targets of different compositions will be necessary. It might be advantageous, if substrate heating and substrate bias are applied as well in order to increase the crystallinity of the deposited films and, thus, to allow a more precise

study of the resulting material properties. The obtained results within this thesis for the as-deposited reactively and non-reactively synthesised molybdenum oxide films can serve as a basis and starting point for future investigations.

ABBREVIATIONS

AMLCD	*A*ctive *M*atrix *L*iquid *C*rystal *D*isplay
AC	*A*lternating *C*urrent
bcc	*B*ody-*C*entred *C*ubi*c*
DC	*D*irect *C*urrent
EDS	*E*nergy *D*ispersive X-Ray *S*pectroscopy
fcc	*F*ace-*C*entred *C*ubic
ICDD	*I*nternational *C*entre for *D*iffraction *D*ata
ITO	*T*in doped *I*ndium *O*xide
m	*M*onoclinic
o	*O*rthorhombic
PDA	*P*ersonal *D*igital *A*ssistant
PVD	*P*hysical *V*apour *D*eposition
RF	*R*adio *F*requency
SEM	*S*canning *E*lectron *M*icroscopy
TCO	*T*ransparent *C*onductive *O*xide
TFT	*T*hin *F*ilm *T*ransistor
WDS	*W*avelength *D*ispersive X-Ray *S*pectroscopy
XRD	*X*-*R*ay *D*iffraction

REFERENCES

[1] **D. A. Figueiredo, H. R. Patil**, *TFT-LCD Panel Fundamentals*, Electronics For You 42 (3), pp. 113–116, March 2010.

[2] **H. K. Pulker**, *Coatings on Glass,* Elsevier, Amsterdam, 2nd edition, 1999.

[3] **A Dietrich, N. Marschall in: G. Kienel (ed.)**, *Vakuum-Beschichtung 5: Anwendungen Teil II*, VDI-Verlag, Düsseldorf, 1993, chapter 6, 7. (in German)

[4] **L. Kihlborg**, *Studies on Molybdenum Oxides*, Acta Chem. Scand. 13 (5), pp. 954–962, 1959.

[5] **H. Gruber, E. Krautz**, *Untersuchungen der elektrischen Leitfähigkeit und des Magnetowiderstandes im System Molbydän-Sauerstoff*, Phys. Status Solidi A 62 (2), pp. 615–624, 1980. (in German)

[6] **L. Kihlborg**, *The Structural Chemistry of the Higher Molybdenum Oxides*, Arkiv För Kemi. 21 (44), pp. 471–495, 1963.

[7] **Y. Bando, Y. Kato, T. Takada**, *Crystal Growth of Molybdenum Oxides by Chemical Transport*, Bull. Inst. Chem. Res., Kyoto Univ. 54 (5), pp. 330–334, 1976.

[8] **D. Manno, M. Di Giulio, A. Serra, T. Siciliano, G. Micocci**, *Physical Properties of Sputtered Molybdenum Oxide Thin Films Suitable for Gas Sensing Applications*, J. Phys. D: Appl. Phys. 35 (3), pp. 228–233, 2002.

[9] **D. Mutschall, K. Holzner, E. Obermeier**, *Sputtered Molybdenum Oxide Thin Films for NH_3 Detection,* Sensor Actuat. B-Chem. 36 (1–3) , pp. 320–324, 1996.

[10] **M. Ferroni, V. Guidi, G. Martinelli, P. Nelli, M. Sacerdoti, G. Sberverglieri**, *Charatcterization of a Molybdenum Oxide Sputtered Thin Film as a Gas Sensor*, Thin Solid Films 307, pp. 148–151, 1997.

[11] **C. Liu, Z. Li, Z. Thang**, *MoO_x Thin Films Deposited by Magnetron Sputtering as an Anode for Aqueous Micro-Supercapacitors*, Sci. Technol. Adv. Mater. 14 (6), 065005, 2013.

[12] **C. Julien, G. A. Nazri, J. P. Guesdon, A. Gorenstein, A. Kehlfa, O. M. Hussain**, *Influence of the Growth Conditions on Electrochemical Features of MoO_3 Film Cathodes in Lithium Microbatteries*, Solid State Ionics 73 (3–4), pp. 319–326, 1994.

[13] **V. Bhosle, A. Tiwari, J. Narayan**, *Epitaxial Growth and Properties of MoO_x ($2 < x < 2.75$) Films*, J. Appl. Phys. 97 (8), 083539, 2005.

[14] **C. V. Ramana, V. V. Atuchin, V. G. Kesler, V. A. Kochubey, L. D. Pokrovsky, V. Shutthanandan, U. Becker, R. C. Ewing**, *Growth and Surface Characterization of Sputter-Deposited Molybdenum Oxide Thin Films*, Appl. Surf. Sci. 253, pp. 5368–5374, 2007.

[15] **G. Franz**, *Oberflächentechnologie mit Niederdruckplasmen*, Springer-Verlag, Berlin, 2nd edition, 1994. (in German)

[16] **R. Haefer**, *Oberflächen- und Dünnschicht-Technologie Teil I*, Springer-Verlag, Berlin, 1987. (in German)

[17] **B. A. Movchan, A. V. Demchishin**, *Study of the Structure and Properties of Thick Vacuum Condensates of Nickel, Titanium, Tungsten, Aluminium Oxide and Zirconium Dioxide*, Phys. Met. Metallogr. 28 (4), pp. 83–90, 1969.

[18] **J. A. Thornton**, *Influence of Apparatus Geometry and Deposition Conditions on the Structure and Topography of Thick Sputtered Coatings,* J. Vac. Sci. Technol. 11 (4), pp. 666–670, 1974.

[19] **R. Messier, A. P. Giri, R. A. Roy**, *Revised Structure Zone Model for Thin Film Physical Structure*, J. Vac. Sci. Technol. A 2 (2), pp. 500–503, 1984.

[20] **F. Rovere**, *Theoretical and Experimental Assessment of Cr-Al-Y-N as Protective Coating for γ-TiAl Based Alloys*, Doctoral Thesis, RWTH Aachen University, Germany, 2009.

[21] **D. Mattox**, *Handbook of Physical Vapor Deposition (PVD) Processing*, Elsevier, Amsterdam, 2nd edition, 2010.

[22] **K. P. Müller**, *Praktische Oberflächentechnik*, Vieweg, Braunschweig, 2nd edition, 1996. (in German)

[23] **M. Ohring**, *The Materials Science of Thin Films*, Academic Press, San Diego, 1992.

[24] **W. Westwood**, *Sputter Deposition*, AVS, New York, 2003.

[25] **L. L. Y. Chang, B. Phillips**, *Phase Relations in Refractory Metal-Oxygen Systems*, J. Am. Ceram. Soc. 52 (10), pp. 527–533, 1969.

[26] **C. Zhang, M. C. Gao, Y. Yang, F. Zhang**, *Thermodynamic Modeling and First-Principles Calculations of the Mo-O System,* CALPHAD 45, pp. 178–187, 2014.

[27] **N. Schönberg**, *On the Existence of a Metallic Molybdenum Oxide*, Acta Chem. Scand. 8 (4), pp. 617–619, 1954.

[28] **K. Swars (ed.)**, *Gmelin Handbuch der Anorganischen Chemie – Molybdän Ergänzungsband Teil B1 Verbindungen,* Springer-Verlag, Berlin, 1975. (in German)

[29] **O. Kubaschewski, E. LL. Evans, C. B. Alcock**, *Metallurgical Thermochemistry*, Pergamon Press, Oxford, 4th edition, pp. 336–337, 1967.

[30] **A. Kumar, B. L. Eyre**, *Grain Boundary Segregation and Intergranular Fracture in Molybdenum*, Proc. R. Soc. Lond. A 370 (1743), pp. 431–458, 1980.

[31] **A. Magnéli**, *Structures of the ReO_3-type with Recurrent Dislocations of Atoms: 'Homologous Series' of Molybdenum and Tungsten Oxides*, Acta Cryst. 6, pp. 495–500, 1955.

[32] **L. Kihlborg, A. Magnéli**, *On the Thermal Decomposition of Molybdenum Trioxide in Vacuo*, Acta Chem. Scand. 91, pp. 471–474, 1955.

[33] **T. Ekström, M. Nygren**, *Ternary Phases with the Mo_5O_{14} Type of Structure – I. A Study of the Molybdenum-Vanadium-Oxygen System*, Acta Chem. Scand. 26 (5), pp. 1827–1835, 1972.

[34] **T. Dutta**, *Nanostructured Transparent Conductive Oxides for Device Applications*, Doctoral Thesis, North Carolina State University, USA, 2011.

[35] **L. Kihlborg**, *Crystal Structure Studies on Mo_5O_{14}, A Compound Exhibiting Two-Dimensional Disorder*, Arkiv För Kemi. 21 (40), pp. 427–437, 1963.

[36] **A. Magnéli, G. Andersson,** *On the MoO_2 Structure*, Acta Chem. Scand. 9 (8), pp. 1378 –1381, 1955.

[37] **http://www.plansee.com/de/Werkstoffe-Molybdaen-402.htm**, October 2014. (in German)

[38] **J. B. Goodenough**, *Metallic Oxides*, Prog. Solid State Chem. 5, pp. 145–399, 1971.

[39] **M. A. K. L. Dissanayake, L. L. Chase**, *Optical Properties of CrO_2, MoO_2, and WO_2 in the range 0.2-6 eV*, Phys. Rev. B 18 (12), pp. 6872–6879, 1978.

[40] **P. F. Carcia, E. M. McCarron III**, *Synthesis and Properties of Thin Film Polymorphs of Molybdenum Trioxide*, Thin Solid Films, 155 (1), pp. 53–63, 1987.

[41] **G. Andersson, A. Magnéli**, *On the Crystal Structure of Molybdenum Trioxide,* Acta Chem. Scand. 4, pp. 793–797, 1950.

[42] **http://en.wikipedia.org/wiki/Molybdenum_trioxide,** October 2014.

[43] **P. A. Cox**, *Transition Metal Oxides – An Introduction to their Electronic Structure and Properties*, Clarendon Press, Oxford, 1992.

[44] **A. Blume**, *Synthese und strukturelle Untersuchungen von Molybdän-, Vanadium- und Wolframoxiden als Referenzverbindungen für die heterogene Katalyse*, Doctoral Thesis, Technische Universität Berlin, Germany, 2004. (in German)

[45] **W. den Boer**, *Active Matrix Liquid Crystal Displays*, Elsevier, Amsterdam, 2005.

[46] **http://www.plasma.com/classroom/what_is_tft_lcd.htm,** October 2014.

[47] **A. List, C. Mitterer, G. Mori J. Winkler, N. Reinfried, W. Knabl**, *Oxidation of Sputtered Thin Films of Molybdenum Alloys at Ambient Conditions,* Proceedings of the 17th Plansee Seminar Vol.1 (eds.: L. S. Sigl, P. Rödhammer, H. Wildner), pp. RM 12/1-12/9, 2009.

[48] **H. Köstenbauer, D. Lorenz, J. Winkler, B. Tseng, G. Jakopic**, *Molybdenum Oxides for Low-Reflectance Thin Films in Touch Applications,* Proceedings of the International Display Manufactoring Conference (IDMC), PH–01*,* 2013*.*

[49] **P. Yeh, C. Gu**, *Optics of Liquid Crystal Displays*, John Wiley & Sons, Hoboken, 2nd edition, 2010.

[50] **C. R. Kagan, P. Andry**, *Thin Film Transistors*, Marcel Dekker, New York, 2003.

[51] **N. Fateh**, *Low-Friction Coatings Based on Lubricious Vanadium Oxides*, Doctoral Thesis, Montanuniversität Leoben, Austria, 2008.

[52] **S. Grasser**, unpublished work, Montanuniversität Leoben, Austria, 2011.

[53] **Compact FullRange™ Gauge Manual PKR 251**, Pfeiffer Vacuum, 2008.

[54] **http://www.idealvac.com/files/manuals/Leybold-ITR90-Gauge-Specs-Data-Sheet01.pdf,** October 2014.

[55] **P. Mayrhofer**, *Materials Science Aspects of Nanocrystalline PVD Hard Coatings,* Doctoral Thesis, Montanuniversität Leoben, Austria, 2001.

[56] **K. Nitzsche**, *Schichtmeßtechnik*, Vogel Buchverlag, Würzburg, 1st edition, 1997. (in German)

[57] **J. Goldstein, D. Newbury, D. Joy, C. Lyman, P. Echlin, E. Lifshin, L. Sawyer, J. Michael**, *Scanning Electron Microscopy and X-Ray Microanalysis*, Springer-Verlag, New York, 3rd edition, 2003.

[58] **D. B. Williams, C. B. Carter**, *Transmission Electron Microscopy – A Textbook for Material Science*, Springer-Verlag, New York, 2nd edition, 2009.

[59] **B. D. Cullity, S. R. Stock**, *Elements of X-Ray Diffraction*, Prentice Hall, Upper Saddle River, 3rd edition, 2001.

[60] **J. Chan, P. Friedberg**, *Four-Point Probe Manual,* The University of California, Berkeley, USA, 2002.

[61] **A. C. Fischer-Cripps**, *Nanoindentation,* Springer-Verlag, New York, 2nd edition, 2004*.*

[62] **W. C. Oliver, G. M. Pharr**, *An Improved Technique for Determining Hardness and Elastic Modulus using Load and Displacement Sensing Indentation Experiments,* J. Mat. Res. 7 (6), pp. 1564–1583, 1992.

[63] **D. Winkler**, *Konzeption und Realisierung eines thermisch unterstützten Messverfahrens zur Bestimmung von Eigenspannungen in dünnen Schichten,* Diploma Thesis, Montanuniversität Leoben, Austria, 1997. (in German)

[64] **G. Stoney**, *The Tension of Metallic Films Deposited by Electrolysis*, Proc. Royal. Soc. London Series A 82 (553), pp. 172–175, 1909.

[65] **http://rruff.info/all/chem=Mo,%20O/display=default/R100218** October 2014.

[66] **http://rruff.info/all/chem=Mo,%20O/display=default/R100217** October 2014.

[67] **L P. Kendig, Z. U. Rek, S. M. Yalisove, J. C. Bilello**, *The Role of Impurities and Microstructure on Residual Stress in Nanoscale Mo Films*, Surf. Coat. Technol. 132, pp. 124–129, 2000.

[68] **J.-V. Faou, E. Barthel, S. Y. Grachev**, *Stress Tuning in Sputter-Deposited MoO_x Films*, Thin Solid Films 527, pp. 222–226, 2013.

[69] **International Centre for Diffraction Data**, 2007, Card 03-065-7442 for bcc-Mo.

[70] **International Centre for Diffraction Data**, 2007, Card 01-088-2331 for fcc-Mo.

[71] **J. Häglund, A. Fernández Guillermet, G. Grimvall, M Körling**, *Theory of Bonding in Transition-Metal Carbides and Nitrides*, Phys. Rev. B 48 (16), pp. 11685–11691, 1993.

[72] **International Centre for Diffraction Data**, 2007, Card 01-072-4534 for m-MoO_2.

[73] **International Centre for Diffraction Data**, 2007, Card 00-035-0609 for o-MoO_3.

[74] **N. Fateh, G. A. Fontalvo, C. Mitterer**, *Structural and Mechanical Properties of DC and Pulsed DC Reactive Magnetron Sputtered V_2O_5 films*, J. Phys. D: Appl. Phys. 40, pp. 7716-7719, 2007.

[75] **A. Magnéli, B. Oughton**, *Studies on the Vanadium Pentoxide-Molybdenum Trioxide System. I. The Relation between the Crystal Structure of the two Oxides*, Acta Chem. Scand. 5, pp. 581-584, 1951.

[76] **A. Magnéli, B. Blomberg**, *Studies on the Vanadium Pentoxide-Molybdenum Trioxide System. II. Phase Analysis*, Acta Chem. Scand. 5, pp. 585-589, 1951.

[77] **P. Balog, D. Orosel, Z. Cancarevic, C. Schön, M. Jansen**, *V_2O_5 Phase Diagram Revisited at High Pressures and High Temperatures*, J. Alloy Compd. 429, pp. 87–98, 2007.

[78] **A. J. Detor, A. M. Hodge, E. Chason, Y. Wang, H. Xu, M. Conyers, A. Nikroo, A. Hamza**, *Stress and Microstructure Evolution in Thick Sputtered Films*, Acta Mater. 57, pp. 2055-2065, 2009.

[79] **H. Köstenbauer, G. A. Fontalvo, M. Kapp, J. Keckes, C. Mitterer**, *Annealing of Intrinsic Stresses in Sputtered TiN Films: The Role of Thickness-Dependent Gradients of Point Defect Density*, Surf. Coat. Technol. 201, pp. 4777-4780, 2007.

[80] **R. Hull (ed.)**, *Properties of Crystalline Silicon*, INSPEC, The Institution of Electrical Engineers, London, p. 153, 1999.